

# Structural mechanism underpinning Thermus oshimai Pif1-mediated G-quadruplex unfolding

Yang-Xue Dai, Hai-Lei Guo, Na-Nv Liu, Wei-Fei Chen, Xia Ai, Hai-Hong Li, Bo Sun, Xi-Miao Hou, Stephane Rety, Xu-Guang Xi

# ▶ To cite this version:

Yang-Xue Dai, Hai-Lei Guo, Na-Nv Liu, Wei-Fei Chen, Xia Ai, et al.. Structural mechanism underpinning Thermus oshimai Pif1-mediated G-quadruplex unfolding. EMBO Reports, 2022, 23 (7), pp.e53874. 10.15252/embr.202153874. hal-03718467

HAL Id: hal-03718467

https://hal.science/hal-03718467

Submitted on 10 Oct 2022

**HAL** is a multi-disciplinary open access archive for the deposit and dissemination of scientific research documents, whether they are published or not. The documents may come from teaching and research institutions in France or abroad, or from public or private research centers.

L'archive ouverte pluridisciplinaire **HAL**, est destinée au dépôt et à la diffusion de documents scientifiques de niveau recherche, publiés ou non, émanant des établissements d'enseignement et de recherche français ou étrangers, des laboratoires publics ou privés.

1	Structural mechanism underpinning Thermus oshimai Pif1-mediated G-quadruplex unfolding
2	Yang-Xue Dai <sup>1†</sup> , Hai-Lei Guo <sup>1†</sup> , Na-Nv Liu <sup>1†</sup> , Wei-Fei Chen <sup>1</sup> , Xia Ai <sup>1</sup> , Hai-Hong Li <sup>1</sup> , Bo Sun <sup>2</sup> , Xi-Miao Hou <sup>1*</sup> ,
3	Stephane Rety <sup>3*</sup> , and Xu-Guang Xi <sup>1, 4*</sup>
4	
5	<sup>1</sup> College of Life Sciences, Northwest A&F University, Yangling, Shaanxi 712100, China;
6	<sup>2</sup> School of Life Science and Technology, ShanghaiTech University, Shanghai 201210, China.
7	<sup>3</sup> Université de Lyon, ENS de Lyon, Université Claude Bernard, CNRS UMR 5239, INSERM U1210, LBMC, 46 allée
8	d'Italie, Site Jacques Monod, 69007, Lyon, France;
9	<sup>4</sup> Université Paris-Saclay, ENS Paris-Saclay, CNRS, LBPA, 91190, Gif-sur-Yvette, France.
10	
11	
12	
13	
14	
15	Footnotes:
16	<sup>†</sup> These authors contributed equally to this work.
17	*To whom correspondence should be addressed. Email: <a href="https://houximiao@nwafu.edu.cn">houximiao@nwafu.edu.cn</a> ; <a href="stephane.rety@ens-lyon.fr">stephane.rety@ens-lyon.fr</a> ;
18	xxi01@ens-cachan.fr.
19	
20	
21	
22	

2

3

4

5

6

7

8

9

10

11

12

13

14

16

17

#### ABSTRACT

G-quadruplexes (G4s) are unusual stable DNA structures that cause genomic instability. To overcome the potential barriers formed by G4s, cells have evolved different families of proteins that unfold G4s. Pif1 is a DNA helicase from Superfamily 1 (SF1) conserved from bacteria to humans with high G4 unwinding activity. Here, we present the first X-ray crystal structure of the *Thermus oshimai* Pif1 (*To*Pif1) complexed with a G4. Our structure reveals that *To*Pif1 recognizes the entire native G4 via a cluster of amino acids at domains 1B/2B which constitute a G4-Recognizing Surface (GRS). The overall structure of the G4 maintains its three-layered propeller-type G4 topology, without significant reorganization of G-tetrads upon protein binding. The three G-tetrads in G4 are recognized by GRS residues mainly through electrostatic, ionic interactions, and hydrogen bonds formed between the GRS residues and the ribose-phosphate backbone. Compared with previously solved structures of SF2 helicases in complex with G4, our structure reveals how helicases from distinct superfamilies adopt different strategies for recognizing and unfolding G4s.

15

Key words: G-quadruplexes; ToPif1, G4-Recognizing Surface, X-ray, structures

#### INTRODUCTION

1

2

3

4

5

6

7

8

9

10

11

12

13

14

15

16

17

18

19

20

21

22

23

24

25

26

27

28

29

30

G-quadruplexes (G4s) are higher-order DNA/RNA structures formed from nucleic acid sequences that contain four stretches of three or more guanines interspaced by at least one random nucleotide (Burge et al., 2006; Castillo Bosch et al., 2014). The G-tetrad module, composed of four guanines, forms a planar structure stabilized by non-canonical Hoogsteen hydrogen bonds in the presence of monovalent cations, such as sodium or potassium (Castillo Bosch et al., 2014; Griffin & Bass, 2018). Genome-wide bioinformatics analyses have revealed the prevalence of G4 motifs in key regulatory regions of the human genome, such as promoters, gene bodies, and untranslated regions (Eddy & Maizels, 2006, 2008; Huppert & Balasubramanian, 2005; Todd et al, 2005; Varshney et al, 2020). Following this prediction, a tremendous increase in cell experimental data has demonstrated that G4 structures indeed exist under physiological conditions and are involved in a variety of biological processes, including telomere maintenance, gene expression, epigenetic regulation, and DNA replication (Maizels & Gray, 2013; Schierer & Henderson, 1994). The high thermodynamic stability of G4s in cells can erect significant barriers to replication fork progression. Therefore, failing to resolve the folded G4s during DNA transactions can cause replication to stall and thus may trigger the rampant genomic instability characteristic of certain cancer cells (De & Michor, 2011; Eddy et al, 2015; Edwards et al, 2014; Fontana & Gahlon, 2020). Cells have evolved the capability of resolving stable G4s with a group of helicases that play important roles in the maintenance of genomic stability in many organisms (Mendoza et al., 2016). Pif1 family helicases, belonging to the superfamily 1 (SF1), are conserved across evolution from bacteria to humans and have been shown to unfold G4, being critical for DNA replication, telomere maintenance, and genome stability (Dahan et al, 2018; Li et al, 2016; Wang et al, 2018). For instance, a recent study has demonstrated that Pif1 helicase promotes break-induced replication in mammalian cells (Li et al, 2021). DNA G4-resolving helicases are also found in superfamily 2 (SF2) in groups such as the XPD family (FANCJ and RTEL1) and the RecQ family of helicases (BLM, WRN, RecQ). FANCJ bearing G4-resolving activity is necessary for DNA replication and has shown a unique substrate specificity for G4 architecture (Bharti et al, 2013; Lee et al, 2021). RecQ helicases have been found to efficiently unfold a variety of G4 DNA structures and play essential roles in DNA repair and telomere maintenance (Singh et al. 2012). Furthermore, mutations in FANCJ, BLM, or WRN are associated with human diseases (Budhathoki et al, 2014; Levitus et al, 2005; Zimmer et al, 2020). Though G4 resolvases have attracted much attention, few solved co-crystal structures in which helicase complexed with G4 are available. The X-ray crystal structure of DHX36 in complex with a Myc-promoter-derived G4 was firstly reported and shows that G4 is captured by a specific DHX36-specific motif (DSM) which bears a signature peptide AKKQ found in FANCJ (Wu & Spies, 2016). Based on DHX36-G4 crystal structures, it was suggested that DSM, in coordination with the helicase core, unfolds the G4 one base at a time in an ATP-hydrolysis-independent manner. Recently, a crystal structure (Voter et al, 2018) solved from a helicase core of a RecQ family helicase (CsRecQ) complexed with oligonucleotides harboring a

2 human telomere sequence revealed that a guanine base within the putative G-tetrad is located at the 5'-gate of the

3 electropositive channel, where the G-base is flipped and sequestrated in a guanine specific pocket (GPS) (Voter et al.,

4 2018). This structure is interpreted to represent a post-catalytic complex of CsRecQ bound to unfolded G4. Therefore,

5 SF2 helicases may use a DSM/AKKQ motif or GSP site for G4 binding/unfolding, but these motifs are not found in Pif1.

6 Though crystal structures of Pifl helicases from Homo sapiens, Saccharomyces cerevisiae, Bacteroides sp, and Thermus

oshimai have been recently solved with different DNA substrates such as ssDNA or replication fork mimic, little is

known about how Pif1 helicases interact with G4 (Dai et al, 2021; Dehghani-Tafti et al, 2019; Lu et al, 2018a; Zhou et al,

2016). Elucidating the molecular mechanism by which Pifl helicase recognizes and unfolds G4 molecules largely

depends on the knowledge of crystal structures. Access to structures that represent a "substrate" complex, intermediates,

and a "product" complex, provides very valuable mechanistic information. Although the helicase-G4 DNA complex

structures of DHX36 (Chen et al, 2018) and CsRecQ (Voter et al., 2018) can be considered as representations of an

intermediate substrate complex (Chen et al., 2018) and a final product complex of helicases (Voter et al., 2018),

respectively, the remaining challenge is to obtain the structure in which the helicases interact with an intact G4 (initial

substrate complex) or to capture the structure of the very first steps leading to the transition state.

7

8

9

10

11

12

13

14

15

17

18

19

20

In this study, we report the X-ray crystal structures solved from the Pif1-family helicase from T. oshimai (ToPif1)

bound to a pre-folded G4 bearing 6-8 nt on both sides of the G-tetrads, thereby mimicking the physiological G4 state

formed during DNA replication. This is the first structural snapshot of a helicase complexed with an integral G4. In

combination with bulk and single molecular fluorescent resonance energy transfer assays (smFRET), our studies

provide new mechanistic insight into how a Pif1-family helicase recognizes, binds, and unfolds G4s.

#### 1 RESULTS

# 2 ToPif1 unfolds G-quadruplexes in an ATP-dependent manner without topological preference

Parallel and antiparallel intramolecular G4s, 12 nt-ssDNA, and 24 bp blunt-end DNA were titrated with increasing concentrations of ToPif1 under equilibrium conditions. The apparent dissociation constant  $(K_{d,app})$  determined from the titration curves (Fig 1A and Table 1) demonstrated that ToPif1 binds both antiparallel (G4<sup>Tel</sup>) and parallel G4s  $(G4^{CEB})$  (Fig EV1A) with similar affinity ( $K_{d,app}$  antipara  $\approx 29.63$  nM ( $G4^{Tel}$ );  $K_{d,app}$  para  $\approx 23.27$  nM ( $G4^{CEB}$ )) without any topological preference. Furthermore, although both the G4 and ssDNA (T12) were bound with essentially the same affinities ( $K_{\rm d,app}^{\rm antipara} \approx 29.63$  nM versus  $K_{\rm d,app}^{\rm ssDNA} \approx 29.12$  nM) (Fig 1A (insert) and Table 1), blunt-end DNA bound ToPif1 very weakly ( $K_{dapp} > 250.00$  nM; Fig 1A (insert) and Table 1). The fact that the apparent dissociation constant of G4 and ssDNA are nearly identical suggests that ToPif1 possesses two independent binding sites for ssDNA and G4, respectively. Indeed, competitive binding assays between the labeled G4 and unlabeled ssDNA demonstrated that labeled G4 binding was not influenced by increasing unlabeled ssDNA and vice versa (Fig EV1B). We then investigated ToPifl-mediated G4-unfolding activities by stopped-flow assay according to the previous report (Liu et al, 2020) with both parallel and antiparallel G4 substrates (Cheng et al, 2018) in the absence or the presence of ATP. The kinetic data were fit to Equation 2 to determine the unfolding amplitude  $(A_m)$  and unfolding rate  $(k_{cat})$  measured with different G4 DNAs (Fig 1B and Table 1). Although unfolding activity is undetectable in the absence of ATP or the presence of the non-hydrolyzable ATP analog (Fig EV1C), the values of unfolding amplitudes (A<sub>m</sub>) and unwinding rates ( $k_{cot}$  (s<sup>-1</sup>)) determined with antiparallel G4s were 1.31-fold and 1.39-fold higher than those determined with parallel G4s, respectively (Fig 1B and Table 1). The calculated p-value (0.001) from the above data is less than 0.01, indicating that the observed differences between parallel and anti-parallel are statistically significant.

To gain mechanistic insight into G4 unfolding and understand the molecular basis underlying the differences in G4 unfolding between the parallel and antiparallel G4s, smFRET assays were performed with G4 DNAs in which the bases near the 5' and 3' sides of G4 were fluorescently labeled. Therefore, its unfolding activity could be sensitively recorded by smFRET time-traces. The smFRET time-trajectories recorded with antiparallel G4s comprising three or four G-tetrads (smG4<sup>AP-424</sup> and sm4G4<sup>AP-333</sup>, respectively) were characterized by a stepwise unfolding procedure, in which the smFRET level successively decreased from E  $\approx$  0.90 to E  $\approx$  0.12, and then finally disappeared due to the escape of the unwound DNA from the coverslip (Fig 1C). This phenomenon has been observed previously in studies of ScPif1 by two different laboratories (Hou et al, 2015; Zhou et al, 2014), and was interpreted as that Pif1 helicase first unfolds G4 from the 5'-lateral G-column, resulting in a G-triplex (G3), then further transforms G3 into a G-hairpin structure and finally completely unwinds the duplex. Interestingly, for parallel G4 and under the same experimental conditions, although 30-35% time-traces (type I) recorded were essentially the same as those observed with antiparallel G4, ~65% smFRET time-traces (type II) for parallel G4 oscillated between E  $\approx$  0.90 to E  $\approx$  0.60 without further decrease before the fluorescence signal bleaching (Fig 1D). Thus, the smFRET assays confirmed that ToPif1 unfolds both parallel and antiparallel G4 using the same mechanism, but with different G4 unfolding efficiencies. The reduced unfolding efficiency in parallel G4 may simply result from the higher thermal stability in the

1 parallel G4 compared with the antiparallel G4 (Figs EV1D and EV1E). We then experimentally address this

2 possibility by determining  $T_{\rm m}$  values of antiparallel (G4<sup>AP-424</sup>) and parallel (G4<sup>P-214</sup>) G4 DNAs using a CD melting

3 assay. The results (Figs EV1D and EV1E) show that  $T_{\rm m}$  values determined with antiparallel G4 (G4<sup>AP-424</sup>) and parallel

4 G4 (G4<sup>P-214</sup>) are 40.1 °C and 43.8 °C, respectively, indicating that the reduced unfolding efficiency in parallel G4 may

5 simply result from the higher thermal stability of parallel G4.

#### The overall structure of ToPif1 in complex with G4

6

7

8

9

10

11

12 13

14

15

16

17 18

19

20

2122

23

24

25

26

27

28

29

30

31 32

33

34

35

36

To probe the structural basis of ToPifl-mediated G4 unfolding, ToPifl was complexed with parallel and antiparallel G4 DNAs flanked at their 5'- and 3'- ends with 6 and 8 nt poly(dT), respectively, mimicking G4s formed at a replication fork (Lee et al., 2021; Lemmens et al, 2015). Only parallel G4 (G4<sup>T6/T8</sup>) in complex with ToPif1 in a 1:2 ratio in the presence of ADP·AIF<sub>4</sub> was crystallized and diffracted to 2.58 Å. The asymmetric unit of the crystal structure contained one G4 that was sandwiched between two ToPif1 molecules (named as molecule a and b) bound to ssDNAs with 5'-3' polarity. The two protein molecules in the asymmetric unit were linked through the DNA substrate and related by a rotation of 102.8°, forming a dumbbell-sharped structure (Fig 2A and B). Molecule a anchored close to the 5'-most G-tetrad and molecule b was bound downstream of the 3'-most G-tetrad. Considering the distance between the binding/unwinding surface constituted by domains 1B/2B and the nearest G-tetrad, in the molecule a, this distance is  $\approx 3.00$  Å with the 5'- most G-tetrad; while in molecule b, the distance with the last Gtetrad at the 3' end is greater than 12.0 Å (Fig 2A and B). Therefore, molecule a in 5' is in an active unwinding state during G4 processing, establishing many interactions with G4, while molecule b in 3' is not positioned for G4 unwinding and establishes few contacts with G4 (Fig 2A and B). The domain folding and the spatial arrangement of the modules in ToPif1 adopt a similar architecture as those observed in the solved crystal structures of ToPif1 (Dai et al., 2021) and other Pif1 family helicases from yeast (Lu et al., 2018a) and Bacteroides species (Zhou et al., 2016). Domains 1A and 2A constitute a deep cleft where ADP·AIF<sub>4</sub> is bound, and domain 2B is composed of an SH3-likedomain and a prominent β-hairpin (loop3) (Figs 2A and B and EV1F-I). Each ToPif1 molecule binds a 6 nt poly(dT) stretch. Molecule a binds T1 to T6, and molecule b binds T22 to T27. The conformation of T2-T5 and T24-T27 are conserved, and they superpose with a root mean square deviation (RMSD) of 1.20 Å, as already shown for ToPifl complexed with several ligands, ssDNA and ss/dsDNA (Dai et al., 2021), thus domain 2B exhibits high conformational flexibility. Structural superposition between molecule a and the previously determined ToPif1 complexed with ss/dsDNA (Dai et al., 2021) on domain 1A demonstrated that the center of mass of domain 2B moves upwards by 5.40 Å and rotates 25.70° upon G4 binding. The domains 2A/1B, the configurations of bound ssDNA and the amino-acid residues involved in ssDNA binding overlap substantially (RMSD = 0.28 Å over 103 residues) (Fig EV2A-F), indicating that domain 2B assumes different conformations to accommodate G4 and double-stranded DNA (dsDNA) binding, respectively. Similarly, superposing molecules a and b on domain 1A shows that G4 binding induced a stable β-hairpin (loop3) formation, and the center of mass of domain 2B in the molecule a moved upwards 5.70 Å, accompanied by 22.90° rotation (Fig 2C), suggesting that domain 2B undergoes a significant conformational adjustment before and after G4 unfolding. G4 is complexed with three K<sup>+</sup> ions: two are located inside G4 between the tetrads and an extra K<sup>+</sup> is on top of the 3' side of G4. This K<sup>+</sup> ion is stabilized by the last tetrad (tetrad III:

- 1 G9·G13·G17·G21), T22, and R448 of ToPif1 molecule b. The overall topology of the G4 structure solved in this
- work is consistent with G4s previously reported in complexed with other proteins. They are characterized by a stack
- 3 of three G-tetrads, and the three short loops containing single thymine cross the grooves of the parallel G4 helix,
- 4 joining the top and bottom G-tetrads in the stack (Fig 2D). ToPif1-G4<sup>T6/T8</sup> crystal structure exhibits a good fit with
- 5 SAXS data (Figs EV3A-E and Table EV3) with a  $\chi^2$  of 1.91, confirming that the conformation observed in the crystal
- 6 state is also the one found in the solution.

#### 7 Structural basis of recognitions and interactions of the entire G-quadruplex and the presumed G-base from the

#### 8 unwound G4

- 9 ToPif1 recognizes the entire G4 through a cluster of amino acids at domains 1B/2B, constituting G4-Recognizing
- 10 Surfaces (GRS) (Fig 2E). Although R419 and R392 interact with G11 and G19 in the 5'-most G-tetrad
- 11  $(G7 \cdot G11 \cdot G15 \cdot G19)$  through cation- $\pi$  interactions, respectively, the sidechain amido group of Q327 interacts with the
- deoxyribose group of G11 through nonbonded contacts (Figs 3A and EV2D). Intriguingly, the negatively charged
- 13 carboxyl group of E397 against the negatively charged oxygen atom on the ribose-phosphate backbone near G7 will
- exert a repulsion force, which may influence the global conformation of the G4 (Fig 3B). Furthermore, the phosphate
- group of G20 in the middle tetrad (G8·G12·G16·G20) is stabilized by R135 (Fig 3C). Two positively charged
- residues, K329 and R150, interact with G9 and G21 in 3'-G-tetrad (G9·G13·G17·G21) through ionic and cation-π
- interactions (Fig 3D). Thus, the residues of GRS form structural clusters which differentially recognize the guanine
  - bases from three different tetrads in the G4. It is therefore plausible that the spatial conformation of G4 is destabilized
- 19 by these interactions, and G4 is efficiently unfolded in coordination with translocation forces derived from ATP
- 20 hydrolysis.

18

- 21 In our ToPif1-G4 complex structure (ToPif1- G4<sup>T6/T8</sup>), the T6 just upstream of the 5'-tetrad is interacting with a cluster
- of amino acids (Fig 4A). T6 also stacks against G19 in the flat 5'-G-tetrad (G7·G11·G15·G19) through a  $\pi$ - $\pi$
- 23 interaction. R392 and V395 are specifically involved in thymine base recognition through hydrogen bonds (R392-T6
- 24 = 2.50 Å and V395-T6 = 2.80 Å). Furthermore, the base configuration is further stabilized by  $\pi$ -π stacking between
- 25 F394 and T6. The residues R355 and R135 interact with the ribose and the phosphodiester of T6, but not its thymine
- base. To determine whether the binding of a guanine base at the T6 position can remodel the conformation of GRS to
- 27 accommodate G-base-specific binding, an ssDNA bearing a G4-forming sequence (GR<sub>17</sub>) was directly complexed
- with ToPif1 without pre-folding (Dai et al., 2021). The crystal structure at a resolution of 2.21 Å demonstrated that the
- 29 global conformation of ToPifl-GR<sub>17</sub> (Dai et al., 2021) is similar to the complex ToPifl-G4<sup>T6/T8</sup> (Fig 4B), except that
- 30 the G4 structure is absent. Structural superposition between the two structures revealed three remarkable features: i)
- 31 the G7 in binary complex (ToPif1-GR<sub>17</sub>) occupies the equivalent spatial position of T6 in ToPif1-G4<sup>T6/T8</sup> (Fig 4C); ii)
- 32 both G7 and T6 flip to the same degree (Fig 4D, ≈113.0°); iii) both the bases and ribose groups of G7 and T6 are
  - bound by the same residues (R392, V395, and R335) with essentially the same conformation, except that residue
- N356 establishes an additional hydrogen bond with the phosphate group of G7 upon its binding (Fig 4D). Therefore,
- 35 if base G7 is considered as the first G base from an unfolded G-tetrad, there is no striking structural reorganization to

- accommodate the binding of G rather than T. Although G7 in GR<sub>17</sub> described here provides a conformation for G4
- 2 being unwound in the first base, other mechanisms may also exist.

17

18

19

20

2122

2324

25

26

27

28

29

30

31

32 33

34

# 3 Mutational analysis of the residues involved in G4 binding and unfolding

4 According to the potential functions in G4 binding or/and unfolding, structurally guided single alanine substitution 5 variants of ToPif1 were purified to homogeneity, including i) the mutants R392A, R135A, and R355A, which interact 6 with the T6/G7 base and/or the ribose/phosphodiester moieties; ii) four variants (Q327A, E397A, R419A, and K329A) 7 involved in the 5'-most G-tetrad; and iii) R135 and R150 involved in the interactions with middle G-tetrad and the 3'-8 most G-tetrad, respectively (Table 2). To make sure that the each given residue mutation does not result in a global 9 conformational change, which will affect ascertain the distinct role of the given residue in G4 binding/unfolding, we 10 first performed circular dichroism (CD) spectroscopy and dynamic light scattering (DLS) assays, which will provide the secondary structure information and hydrodynamic behavior (monomer or aggregation) of the variants. The results 11 show that the variants displayed the same CD spectra as ToPif1, and the determined DLS parameters are essentially 12 13 the same between ToPif1 and variants (Fig EV4A and Table EV4). The DNA-dependent ATPase activities of the ToPif1 variants were measured using a coupled spectrophotometric ATPase assay. Fig EV4B and Table EV4 14 demonstrated the determined  $K_{\rm m}$  and  $k_{\rm cat}$  values with the variants are not significantly different from those determined 15 16 with the wild-type *To*Pif1.

To ascertain qualitatively how the modified residues affect the unfolding activities, the  $K_{d,app}$  values, and the steadystate kinetic parameters, including the unfolding magnitude  $(A_m)$  and the unfolding rate  $(k_{cat})$ , were determined with fluorescent-labeled ssDNA (T<sub>12</sub>), partial duplex DNA (S<sub>26</sub>D<sub>17</sub>), and G4 DNA substrates as described above. Several representative G4 unfolding kinetic curves are shown in Fig 5A and the kinetic parameters of all variants are summarized in Table 2. The parameters ( $K_{d,app}$ ,  $A_m$ , and  $k_{cat}$ ) determined with G4 and ssDNA substrates showed a range of variability. To best understand the mutation results, the ratio of  $k_{\text{cat}}/K_{\text{d,app}}$ , a useful index for comparing the catalytic efficiency (Barlow et al, 2009), was determined (Table 2). Arranging the G4 k<sub>cat</sub>/K<sub>d,app</sub> values in ascending numerical order shows that the relative increase in G4  $k_{cat}/K_{d,app}$  values can be roughly classified into three categories (Fig 5B): i) group I (R355A, R135A, and R150A) is characterized by zero values in  $k_{\text{cat}}/K_{\text{d,app}}$  for G4 unfolding while their  $k_{\text{cat}}/K_{\text{d,app}}$  values determined from dsDNA unwinding are reduced by 33% (R150A) and 75% (R355A); ii) group II (R392A, Q327A, K329A, and R419A) is marked by about 44-69% reduction in  $k_{cat}/K_{d,app}$  values for G4 unfolding and the corresponding values determined with dsDNA are essentially the same as these determined with ToPif1, except that  $k_{\text{cat}}/K_{\text{d,app}}$  value determined with R419A for dsDNA is reduced to 50%; iii) group III (E397A, E397L, and E397H) displays surprising results in which k<sub>cat</sub>/K<sub>d,app</sub> values determined with G4 are increased to 2-2.6 folds while the  $k_{\text{cat}}/K_{\text{d,app}}$  values for dsDNA are inversely reduced to 50% compared with that of ToPif1. Taken together, these results indicate that alteration of the residues in group I-II, particularly the residues in group I, significantly impair G4 unfolding, but only moderately reduces dsDNA unwinding. Consistently, smFRET time trajectories recorded with the mutants in group III revealed that in sharp contrast to wtToPif1, the curves only oscillate between 0.90 and 0.60, but

- scarcely attain a completely unfolded level, indicating that the variants can just release the 5'-most lateral G column
- 2 from G4 DNA, but is unable to unfold the integral G4 DNA completely (Fig 5C-F).
- 3 In group III, the kinetic parameters determined with E397A were significantly higher in terms of unfolding amplitude
- 4  $(A_{\rm m})$  and rate  $(k_{\rm cat})$ , respectively (Figs 5B and 6A and Table 2). Compared with  $T_0$ Pif1, the  $k_{\rm cat}/K_{\rm d,app}$  value of E397A
- 5 determined for G4 unfolding increased by 2.5-fold, although that for dsDNA remained unchanged (Table 2). This
- 6 stimulation effect was also observed with parallel G4s (Fig 6B). To confirm this interpretation, residue E397 was
- 7 therefore replaced with a hydrophobic (E397L), a positively charged (E397H), and a negatively charged (E397D)
- 8 residue. As expected, G4 unfolding activities determined with the first two variants were systematically higher than
- 9 those of ToPif1. E397D bearing a negative charge displayed activity comparable to the wild type (Fig 6A). To gain in-
- depth mechanistic insight into how residue E397 affects G4-unfolding activity, all of the variants were further studied
- 11 with smFRET techniques. Analysis of the smFRET time-traces demonstrated that the unfolding times (t(s))
- determined with the three typical variants were significantly reduced, except those for E397D, whose unfolding time
- 13 remained essentially the same as that of ToPifl (Fig 6C-F). The mutation-stimulating G4-resolution activity is
- 14 surprising and raises the question of whether this may be a general autoregulatory mechanism by which the activity of
- 15 G4 unfolding is regulated both *in vitro* and *in vivo*.

#### DISCUSSION

- While increasing evidence has demonstrated that helicase-mediated G-quadruplex unfolding plays an essential role in
- 18 preserving genome stability, the lack of structural information on G4-processing helicases still hampers our
- 19 mechanistic understanding of G4 resolution. With a wide array of approaches ranging from bulk/smFRET assays to
- 20 structural biology analyses, our results reported here provide in-depth insight into the currently largely unknown, but
- 21 mechanistically important issue of how the Pif1 helicase family recognizes the integral G4 structure.
- 22 To our best knowledge, the structure reported here is the first co-crystal structure of SF1 helicase bound to G4, while
- 23 crystal structures of SF2 helicase-G4 complexes available are DHX36 and CsRecQ proteins. Thus, a structural
- 24 comparison between SF1 and SF2 helicase-mediated G4 binding/unfolding may provide the common and distinct
- 25 mechanism underlying G4 unfolding.
- 26 DHX36 protein, one of the most extensively studied G4-unfolding helicases, is characterized by a DHX36-specific motif
- 27 (DSM), which specifically binds parallel G4s (Hossain et al., 2021). Interestingly, the X-ray crystal structure of DHX36
- 28 (Chen et al., 2018) in complex with a Myc-promoter-derived G4 demonstrates a rearrangement of the 5'-G-tetrad with a
- one-base translocation upon DSM binding (Chen et al., 2018). Because an NMR study shows that G4 keeps its integral
- 30 state upon the binding of an isolated DSM (Heddi et al, 2015), it was, therefore, suggested that DSM, in coordination
- 31 with the helicase core, unfolds the G4 one base at a time in an ATP- hydrolysis-independent manner (Chen et al., 2018).
- 32 Recently, a crystal structure solved from a helicase core of a RecQ family helicase (CsRecQ) complexed with

oligonucleotides harboring a human telomere sequence (Voter et al., 2018) revealed that a guanine base within the 1 putative G-tetrad is located at the 5'-gate of the electropositive channel where the G-base is flipped and sequestrated 2 (Voter et al., 2018). This structure is interpreted to represent "a product complex of CsRecQ-unwound G4 rather than a 3 folded quadruplex" (Voter et al., 2018) although the complexed ssDNA was not pre-folded to form a stable G4 before the 4 5 preparation of the G4-CsRecQ complex. 6 DHX36 uses DSM to bind and unfold G4s, and some G4-resolving helicases as FANCJ also possess a motif equivalent to 7 DSM (Chen et al., 2018; Lee et al., 2021). However, not all the SF2 helicases bear DSM. An intriguing and unresolved 8 question is how the G4-resolving helicases generally recognize and unfold G4s. We demonstrated that the 1B/2B domains 9 in ToPif1 constitute a G4-Recognizing Surface (GRS) in which the residues recognize the whole G4 structure, not just a tetrad, and differentially interact with the ribose and phosphate units in different tetrads. Superposition of the structural 10 11 conformation of G4 complexed with ToPif1 with that of the DHX36-Myc complex (Chen et al., 2018) demonstrated that, when the G4s well superposed, loop3 in ToPif1 occupies the spatial position of the DSM motif in DHX36, binding on the 12 5' side of the G4. Given that Pif1 and DHX36 have opposite polarity for ssDNA translocation, it appears that helicase 13 14 binding on the 5' side of G4 is a critical feature for G4 unwinding. Furthermore, it appears that the previously identified 15 GSP in the RecQ helicase family is not conserved in ToPif1, because the residues involved in the first base downstream of 5'-G-tetrad are not selective for guanine and do not form the equivalent hydrogen bonds that stabilize the guanines within 16 G4s as observed in GSPs (Figs 4A-D and EV4C-E). If base G7 is considered as the first G base from an unfolded G-tetrad, 17 there is no striking structural reorganization to accommodate the binding of G rather than T. Compared with the 18 previously identified GSP, the cluster of residues surrounding the base (T6/G7) upstream of the G-tetrad in ToPif1 are not 19 bound with the equivalent residues identified in the GSP in CsRecQ (Fig EV4C-E). Of note, the G-rich ssDNA (GR<sub>17</sub> 20 21 (Dai et al., 2021) and resolved G4 DNA (Voter et al., 2018)) were not pre-folded to form stable G4 DNA in the ToPif1 22 and CsRecQ structures; it, therefore, remains to be determined whether these structures (ToPif1-GR<sub>17</sub> (Dai et al., 2021) 23 and CsRecQ-ssDNA (Voter et al., 2018)) represent an intermediate or/and a product complex of helicases bound to unwound G4 DNA or just ssDNA bound to the proteins. 24 Our binding studies demonstrated that ToPifl possesses strong G4 binding activity without any topological preference. 25 This is not surprising because ToPifl does not bear a DSM motif which was reported exclusively bind parallel G4 26 (Hossain et al., 2021). The smFRET time-trajectory feature of ToPif1-mediated G4 unfolding is mainly characterized by a 27 stepwise unfolding procedure, without a long oscillation period, which is consistent with the previously recorded 28 29 smFRET time-trajectory with ScPif1 (Hou et al., 2015; Zhou et al., 2014). These results imply that ToPif1 translocates along the DNA lattice and sequentially unfolds G4 into G-triplexes and then into G-hairpins. ToPif1-mediated G4 30

processing is radically different from previous reports on DHX36 (Chen et al., 2018) and the RecQ (Voter et al., 2018) helicase family, which were shown to use a common mechanism of ATP-independent repetitive unfolding to resolve G4s: binding of these helicases triggers the reorganization and destabilization of G4 with a one-at-a-time type base translocation, and ATP is only needed for releasing the unfolded G4 (Chen et al., 2018; Voter et al., 2018). Therefore it appears that SF1 helicases unfold G4 in a stepwise manner while SF2 helicases unfold G4 repetitively; however, establishing these observations as a general rule needs further studies. Another interesting finding is that two negative charges between E397 and the oxygen atom on the DNA backbone near G7 repel one another. A series of mutations at E397 demonstrated that replacement of the negative residue by any non-negative residue stimulates G4 unfolding activity, raising the question that whether an auto-inhibitory mechanism applies to other ToPif1 helicases. A sequence alignment of Pif1 family helicases revealed that a negative residue (E/D) is highly conserved in thermophilic gram-negative bacteria (Fig EV5). However, there is a tendency towards replacing negative residue (E/D) with no-negative residues (S/G) in evolutionarily advanced species (Fig EV5). Therefore it appears that ToPif1 has not evolved with an optimum efficiency, but this could be due to growth conditions, G4 frequency in the genome, or a yet unknown regulatory mechanism stimulating *ToPif1* activity. The relation between growth temperature, G4 frequency, and Pifl efficiency is not straightforward. Analysis of the occurrence of putative G4 sequences (PQS) in bacteria has recently been conducted. Though thermophile bacteria have genomes with higher GC content, the distribution of POS is higher than expected by random chance in bacteria groups Deinococcales and Thermales while using either quadparser (Ding et al, 2018) or G4hunter (Bartas et al, 2019) algorithms. In later study, it was shown that T. oshimai had the highest frequency of PQS among all bacterial genomes explored (Table EV5). Surprisingly, the same study showed that *Thermotogae* which are also extremely thermophilic gram-negative bacteria, have the lowest frequency of PQS (Table EV5). Therefore, G4 occurrence does not seem to be linked to thermal conditions of growth. Bacteria from Thermotoga group possess also a Pif1 helicase which exhibits G4 activity (Andis et al, 2018). The biochemical activities of Pifl from Thermotoga elfi (TePifl) have been measured, and TePif1 exhibits a C-terminal WYL domain with ssDNA binding function (Andis et al., 2018) necessary for substrate binding and helicase activity of TePifl. WYL domain is shared by Pifl from other groups, such as Deferribacteres, but ToPif1 does not have one. Since Pif1 from other thermophilic bacteria such as Thermotoga elfii possessed an extra WYL domain (Andis et al., 2018), modulation of Pif1 activity in cis (WYL domain) and a regulatory effect on Pif1 in trans by unidentified co-factor proteins can be hypothesized.

1

2

3

4

5

6

7

8

9

10

11

12

13

14

15

16

17

18

19

20

21

22

23

24

25

26

27

It was recently reported that the proteins Mgs1 and Mms1 in *S. cerevisiae* binding to G4 motifs *in vivo* partially depends on the helicase *Sc*Pif1 (Paeschke & Burkovics, 2021; Schwindt & Paeschke, 2018). Using the sequence similarity search tool, we identified the Mgs1-like protein in *Thermus oshimai* genome (*To*Mgs1 like, Genebank: WP\_018462088.1) which share shares 29% identity with *Sc*Mgs1 across their lengths. *To*Mgs1 could be a co-factor regulating *To*Pif1 in trans.

Though Pif1 is conserved from bacteria to humans, Pif1 has very diverse functions in bacteria, yeast, and human. Pif1 sequence exhibits variations with the insertion domain 2C in budding yeast (Lu *et al.*, 2018a) (Lu *et al.*, 2021) and accessory domains as WYL (Andis *et al.*, 2018). Furthermore, sequence alignments show that some of the key residues identified in GRS are shared with other bacteria but not with Pif1 from eukaryotes (for an alignment, see Fig S1 in Supplementary material in (Dai *et al.*, 2021)). We show here that *To*Pif1 can rely only on its helicase core domain to recognize and unfold G4 DNA while the activity of *Te*Pif1 needs a WYL accessory domain (Andis *et al.*, 2018).

Therefore, it appears that Pif1 from different species adopts different solutions for enhancing its activity. Thus, co-factors

acting in cis or trans may enhance Pif1 activity for certain species, and the situation is far from being universal even in the

Bacteria domain. Further studies, instigated by the work reported here, are needed to complete our understanding of the

general mechanism underlying how G4-resolving helicases recognize and unfold G4s.

#### MATERIALS AND METHODS

#### 2 Reagents and buffers

1

7

15

- 3 All chemicals were reagent grade and all buffers were prepared in high-quality deionized water from a Milli-Q ultrapure
- water purification system (Millipore) with a resistivity of >18.2 M $\Omega$ .cm and were filtered again on a 0.20  $\mu$ m filter
- before use. All DNA unwinding and binding assays were performed in buffer A (20 mM Tris-HCl (pH 7.5 at 37 °C), 50
- 6 mM NaCl, 2 mM MgCl<sub>2</sub>, 2 mM DTT) which was optimized previously by our group (Dai et al., 2021).

### DNA substrate preparation

- 8 All the DNA substrates used in this study were chemically synthesized and HPLC-purified by Sangon Biotech
- 9 (Shanghai) as listed in Table EV1. The oligonucleotides used in binding and unwinding assays were prepared at a 2 μM
- working concentration. The duplex or G4 DNA used in the stopped-flow and smFRET assays were heated to 95 °C for 5
- min in stocking buffer (20 mM Tris-HCl, pH 7.5, 100 mM NaCl) and annealed by slow cooling to room temperature.
- 12 The DNA substrates in crystallization were dissolved in 20 mM Tris-HCl (pH 7.5) with 100 mM KCl, heated to 95 °C,
- and allowed to cool slowly to room temperature in a water bath. After purification on a Mono Q column, the formation
- of G4 structures was checked using circular dichroism (CD) spectropolarimetry.

#### Protein expression and purification

- 16 ToPif1 (residues 64-507) and its mutants (R355A, R135A, R150A, R419A, R392A, Q327A, K329A, E397A, E397L,
- 17 E397H, and E397D) were all cloned into pET15b-SUMO and then transformed into the C2566H E. coli strain (New
- England Biolabs), respectively. When the culture reached the early stationary phase ( $OD_{600} = 0.55 0.6$ ) at 37 °C, 0.3
- 19 mM IPTG was added and the protein expression was induced at 18 °C over 16 h. Cells were harvested by centrifugation
- 20 (4500 g, 4 °C, 15 min) and pellets were suspended in lysis buffer (20 mM Tris-HCl pH 7.5, 500 mM NaCl, 10 mM
- 21 Imidazole, and 5% glycerol (v/v)). Cells were broken with a French press and then further sonicated 2-3 times to shear
- DNA. After centrifugation at 12,000 rpm for 40 min, the supernatants were filtered through a 0.45-µm filter and loaded
- onto a Ni<sup>2+</sup> charged IMAC column (GE Healthcare). After washing twice, the SUMO-ToPif1 was then eluted from the
- Ni<sup>2+</sup> affinity column with elution buffer (20 mM Tris-HCl, pH 7.5, 500 mM NaCl, 300 mM Imidazole, and 5% glycerol
- 25 (v/v)) at 4 °C. The eluted protein was treated with SUMO protease (Invitrogen, Beijing). Then the SUMO digested
- 26 protein was further purified by a HiTrap Heparin column (GE Healthcare) to remove the SUMO-tag and other protein
- 27 impurities. The eluted fraction containing ToPifl was collected and concentrated. The final purified protein was dialyzed
- against the storage buffer (20 mM Tris-HCl, pH 7.5, 500 mM NaCl, 1 mM DTT) and concentrated to approximately 10

- 1 mg/mL for crystallization, and was about 95% pure as determined by SDS-PAGE. Mutations and truncations were
- 2 engineered by PCR overlapping-PCR protocol.

#### 3 Equilibrium binding assays

- 4 The isothermal binding curves were determined using a fluorescence polarization assay on an Infinite F200 plate reader
- 5 (Tecan). FAM-labeled DNA substrates were used in this study. Varying amounts of protein were added to a 150 μL
- 6 aliquot of buffer A containing 5 nM FAM-labeled DNA. Each sample was allowed to equilibrate in solution for 5 min at
- 7 37 °C, and then fluorescence polarization was measured. Less than 5% change was observed between the 5 and 10 min
- 8 measurements, indicating that equilibrium was reached in 5 min. The equilibrium dissociation constants were
- 9 determined by fitting the binding curves using Equation 1:

$$\Delta r = \Delta r_{\text{max}} \times P / (K_{d.app} + P) \tag{1}$$

- where  $\Delta r_{\text{max}}$  is the maximal amplitude of the anisotropy (i.e.,  $r_{\text{max}} r_{\text{free,DNA}}$ ), P is the helicase concentration, and  $K_{\text{d,app}}$  is
- the midpoint of the curve corresponding to the apparent dissociation constant.

#### Crystallization of ToPif1-nucleic acid complexes

- For crystallization, purified ToPif1 was incubated with the G4<sup>T6/T8</sup> after dissolving and folding in 20 mM Tris-HCl (pH
- 7.5) with 100 mM KCl at a molar ratio of 2:1 in the presence of ATP analog ADP·AlF<sub>4</sub>. The resulting *To*Pifl-G4<sup>T6/T8</sup>-
- 16 ADP·AlF<sub>4</sub> complex was purified using size-exclusion chromatography and then concentrated to approximately 10
- mg/mL. Crystallization trials on ToPif1 and its complexes with DNA (Table EV1) and ADP·AlF<sub>4</sub> were performed at
- 18 20 °C using the sitting-drop vapor diffusion method. Crystallization screening was carried out at 20 °C using
- 19 commercial screening kits (Hampton Research, Molecular Dimensions, and Rigaku Reagents), where the ToPifl-DNA
- complex was mixed at a 1:1 ratio with the reservoir solution. Crystals of ToPif1-G4<sup>T6/T8</sup>-ADP·AlF<sub>4</sub> were obtained using
- 21 0.1 M Bis-Tris (pH = 6.5), 10% PEG20000. All these conditions were optimized with a grid search using 48-well Linbro
- 22 plates at 20 °C, where 1 μL of protein sample and 1 μL of precipitant were mixed and equilibrated with 60 μL of
- 23 precipitant.

24

13

#### X-ray data collection, phasing, and refinement

- 25 All X-ray diffraction data were collected on beamline BL19U1 (Zhang et al, 2019) at the Shanghai Synchrotron
- 26 Radiation Facility (China) using a Pilatus 6M detector (Dectris) and were processed using XDS (Kabsch, 2010). ToPif1-
- 27 G4<sup>T6/T8</sup>-ADP·AlF<sub>4</sub> structures were solved by molecular replacement, performed in the PHENIX software suite (Adams

et al, 2010) with Phaser (McCoy et al, 2007), using the ToPif1 apo structure (PDB: 6S3E (Dai et al., 2021)) as the

2 search model (Lovelace et al, 2005). Manual rebuilding was done using the Coot (Emsley et al, 2010) and further

3 refinement was performed in PHENIX. Cell parameters and data collection statistics are reported in Table EV2.

#### Small-angle X-ray scattering assay

4

15

16

17

18

19

20

21

22

23

24

25

26

SEC-SAXS experiment was carried out at beamline SWING (SOLEIL Synchrotron, Saint-Aubin, France) with SEC-5 6 HPLC coupled to SAXS. The sample of ToPif1-G4 complex was injected at a concentration of 10 mg/ml on a Superdex 7 200 5/150 Increase column (Cytiva) at a flow rate of 0.2 ml/min equilibrated in buffer 25 mM Hepes (pH=7.5), 150 mM KCl, 5% glycerol. Scattering data were collected at 20 °C using a Pilatus 1M detector (Dectris), and the data reduction 8 9 and processing of images were done with Foxtrot (David & Pérez, 2009). Further analysis was done with ATSAS 2.8 suite (Petoukhov et al, 2012). Experimental  $R_g$ , I(0), and  $D_{max}$  values were calculated with PRIMUS and GNOM4 10 programs respectively. Ab initio envelopes for isolated complexes were determined using DAMMIF with the pair 11 12 distance distribution function calculated with GNOM4. Full atomic models derived from crystal structure were modeled 13 with MODELLER and adjusted to SAXS data with DADIMODO. In this modeling procedure, only the missing parts 14 from the X-ray structure were kept flexible. Profiles of atomic models were calculated and fitted to the experimental data

using CRYSOL and aligned on ab initio bead models with SUPCOMB. All the SAXS parameters are summarized in

#### Stopped-flow unwinding assay

Table EV3.

Briefly, unwinding kinetics were measured in a two-syringe mode, where *To*Pifl and fluorescently labeled DNA substrate were pre-incubated at 37 °C in one syringe for 5 min and the unwinding reaction was initiated by rapidly mixing with ATP from another syringe. Each syringe contained unwinding reaction buffer A (25 mM Tris-HCl (pH 7.5), 50 mM NaCl, 2 mM MgCl<sub>2</sub> and 2 mM DTT). All concentrations listed are after mixing, unless otherwise noted. For converting the output data from volts to percentage unwinding, a calibration experiment was performed in a four-syringe mode, where the helicase, the hexachlorofluorescein-labeled single-stranded oligonucleotides, the fluorescein-labeled single-stranded oligonucleotides, and ATP were in four syringes, respectively. The fluorescent signal of the mixed solution from the four syringes corresponded to 100% unwinding. The standard reaction was performed with 4 nM DNA substrates, 1 mM ATP, and 100 nM *To*Pifl in buffer A.

All stopped-flow kinetic traces were averages of ≥10 individual traces. The kinetic traces were analyzed using Bio-Kine (version 4.26, Bio-Logic, France) using Equation 2:

29 
$$A(t) = A_1(1 - e^{-k_1(t-t_0)}) + A_2(1 - e^{-k_2(t-t_0)})$$
 (2),

- where A(t) represents the fraction of DNA unwound at time t,  $A_1$  and  $A_2$  are the unwinding amplitudes,  $k_1$  and  $k_2$  are the
- 2 unwinding rate constants of the two phases,  $t_0$  is the time at which the fraction of DNA unwound starts to rise. From the
- 3 four parameters obtained through the fitting, we can determine the total unwinding amplitude  $A_{\rm m} = A_1 + A_2$  and the initial
- 4 unwinding rate (i.e., the slope of the kinetic unwinding curve at early times)  $k_{\text{cat}} = k_1 A_1 + k_2 A_2$ .

#### Single-molecule fluorescence data acquisition

5

13

- 6 50 pM fluorescently labeled DNA was added to the chamber containing imaging buffer composed of 20 mM Tris-HCl
- 7 (pH 7.5), 1 mM MgCl<sub>2</sub>, 50 mM NaCl, 1 mM DTT and an oxygen scavenging system (0.8% D-glucose, 1 mg/mL
- 8 glucose oxidase, 0.4 mg/mL catalase and 1 mM Trolox). After immobilization for 10 min, free DNA molecules were
- 9 removed by washing with the imagining buffer. We used an exposure time of 100 ms for all recordings at a constant
- 10 temperature of 22 °C. FRET efficiency was calculated using  $I_A/(I_D + I_A)$ , where  $I_D$  and  $I_A$  represent the intensities of
- donor and acceptor, respectively. Basic data analysis was carried out by scripts written in MATLAB, and all data fitting
- were generated using Origin 9.0. Histograms were fitted to Gaussian distributions, with the peak positions unrestrained.

#### Circular dichroism spectropolarimetry

- 14 Circular dichroism (CD) experiments were performed with a Bio-Logic MOS450/AF-CD optical system (BioLogic
- 15 Science Instruments, France) equipped with a temperature-controlled cell holder, using a quartz cell with a 1-mm path
- 16 length. A 2.5 μM solution of G4 DNA was prepared in 25 mM Tris-HCl (pH 7.5), 100 mM NaCl. CD spectra were
- 17 recorded in the UV (220–320 nm) regions in 0.75 nm increments with an averaging time of 2 s at 25°C.

#### 18 Dynamic light scattering (DLS) assay

- 19 DLS measurements were performed at 37°C using a DynaPro NanoStar instrument (Wyatt Technology Europe GmbH,
- 20 Germany) equipped with a thermostated cell holder and disposable cuvettes (UVette, Eppendorf). All solutions were
- 21 filtered using 0.22 μm filters. Purified ToPifl or its mutants (10 μM) was dialyzed in buffer A (final volume, 30 μl). The
- scattered light was collected at an angle of 90°. Recording times were typically between 3-5 min (20-30 cycles in
- average, 10 s in each cycle). The analysis was performed with the Dynamics 7.0 software using regularization method
- 24 (Wyatt Technology). The molecular weight was calculated from the hydrodynamic radius using the following empirical
- 25 Equation 1,

28

$$Mw = (1.68 \times R_{\rm H})^{2.34} \tag{1}$$

where Mw and  $R_{\rm H}$  represent the molecular weight (in kDa) and the hydrodynamic radius (in nm), respectively.

#### ATP hydrolysis measurement

- 1 The malachite green assay (MAK113; Sigma-Aldrich) was used to test the ATP hydrolysis activity of ToPif1 and its
- 2 mutants by measuring the release of inorganic phosphate as previously described (Liu et al, 2021; Mahieu et al, 2020).
- 3 Briefly, 100 nM purified protein and ATP (concentrations ranging from 0 μM to 400 μM) were incubated with or without
- 4 1 mM DNA effector (S<sub>18</sub>H<sub>11</sub>, sequence were shown in Table S1) using a VICTOR Nivo Multimode Microplate Reader
- 5 (PerkinElmer, Waltham, MA, USA). All reactions were performed in triplicates of 150 μL each at 25°C in buffer A. The
- 6 parameters of  $K_{\rm m}$  and  $k_{\rm cat}$  were calculated by fitting the experimental data to the Michaelis–Menten equation using Origin
- 7 9.0 (OriginLab Corporation, Northampton, MA, USA).

#### 8 DATA AVAILABILITY

- 9 Accession codes: The atomic coordinate and structure factors have been deposited in the Protein Data Bank
- 10 (https://www.rcsb.org/) with the following accession numbers: 7OAR (*To*Pif1-G4<sup>T6/T8</sup>-ADP·AlF<sub>4</sub>).
- 11 **Expanded View** for this article is available online.

#### 12 ACKNOWLEDGEMENTS

- We are grateful for access to the SOLEIL (SWING) synchrotron radiation facility for SAXS data collections. We
- thank the staffs from BL17U1/BL18U1/BL19U1 beamline of National Facility for Protein Science in Shanghai
- 15 (NFPS) at Shanghai Synchrotron Radiation Facility, for assistance during data collection. This work was supported
- by National Natural Science Foundation of China [31870788, 11574252, 11774407]; the Natural Science Basic
- 17 Research Program of Shaanxi (2020JQ-251); CNRS LIA ('Helicase-mediated G-quadruplex DNA unwinding and
- 18 genome stability'). Funding for open access charge: National Natural Science Foundation of China [31870788].

#### 19 Author contributions

- 20 Conceived and designed study: XGX, XMH, and SR. Experiments: YXD, HLG, NNL, WFC, XA, and HHL. Data
- 21 processing: YXD, NNL, WFC, and HLG. Discussion and interpretation of data: XGX, XMH, WFC, and SR.
- 22 Manuscript writing and editing: XGX, YXD, NNL, BS, and SR, with input from all authors.
- 23 Disclosure and competing interest statement. None declared.

#### 1 REFERENCES

- 2 Adams PD, Afonine PV, Bunkoczi G, Chen VB, Davis IW, Echols N, Headd JJ, Hung LW, Kapral GJ, Grosse-Kunstleve RW et
- 3 al (2010) PHENIX: a comprehensive Python-based system for macromolecular structure solution. Acta crystallographica
- 4 Section D, Biological crystallography 66: 213-221
- 5 Andis NM, Sausen CW, Alladin A, Bochman ML (2018) The WYL Domain of the PIF1 Helicase from the Thermophilic
- 6 Bacterium Thermotoga elfii is an Accessory Single-Stranded DNA Binding Module. *Biochemistry* 57: 1108-1118
- 7 Barlow JN, Conrath K, Steyaert J (2009) Substrate-dependent modulation of enzyme activity by allosteric effector
- 8 antibodies. *Biochimica et biophysica acta* 1794: 1259-1268
- 9 Bartas M, Cutova M, Brazda V, Kaura P, Stastny J, Kolomaznik J, Coufal J, Goswami P, Cerven J, Pecinka P (2019) The
- 10 Presence and Localization of G-Quadruplex Forming Sequences in the Domain of Bacteria. Molecules 24
- 11 Bharti SK, Sommers JA, George F, Kuper J, Hamon F, Shin-ya K, Teulade-Fichou MP, Kisker C, Brosh RM, Jr. (2013)
- 12 Specialization among iron-sulfur cluster helicases to resolve G-quadruplex DNA structures that threaten genomic
- stability. *The Journal of biological chemistry* 288: 28217-28229
- Budhathoki JB, Ray S, Urban V, Janscak P, Yodh JG, Balci H (2014) RecQ-core of BLM unfolds telomeric G-quadruplex in
- the absence of ATP. *Nucleic Acids Res* 42: 11528-11545
- 16 Burge S, Parkinson GN, Hazel P, Todd AK, Neidle S (2006) Quadruplex DNA: sequence, topology and structure. *Nucleic*
- 17 Acids Res 34: 5402-5415
- 18 Castillo Bosch P, Segura-Bayona S, Koole W, van Heteren JT, Dewar JM, Tijsterman M, Knipscheer P (2014) FANCJ
- 19 promotes DNA synthesis through G-quadruplex structures. *Embo j* 33: 2521-2533
- 20 Chen MC, Tippana R, Demeshkina NA, Murat P, Balasubramanian S, Myong S, Ferré-D'Amaré AR (2018) Structural basis
- 21 of G-quadruplex unfolding by the DEAH/RHA helicase DHX36. *Nature* 558: 465-469
- 22 Cheng M, Cheng Y, Hao J, Jia G, Zhou J, Mergny JL, Li C (2018) Loop permutation affects the topology and stability of G-
- 23 quadruplexes. *Nucleic Acids Res* 46: 9264-9275
- 24 Dahan D, Tsirkas I, Dovrat D, Sparks MA, Singh SP, Galletto R, Aharoni A (2018) Pif1 is essential for efficient replisome
- 25 progression through lagging strand G-quadruplex DNA secondary structures. Nucleic Acids Res 46: 11847-11857
- 26 Dai YX, Chen WF, Liu NN, Teng FY, Guo HL, Hou XM, Dou SX, Rety S, Xi XG (2021) Structural and functional studies of
- 27 SF1B Pif1 from Thermus oshimai reveal dimerization-induced helicase inhibition. *Nucleic Acids Res* 49: 4129-4143
- David G, Pérez J (2009) Combined sampler robot and high-performance liquid chromatography: a fully automated
- 29 system for biological small-angle X-ray scattering experiments at the Synchrotron SOLEIL SWING beamline. Journal of
- 30 Applied Crystallography 42: 892-900
- 31 De S, Michor F (2011) DNA secondary structures and epigenetic determinants of cancer genome evolution. *Nature*
- 32 structural & molecular biology 18: 950-955
- 33 Dehghani-Tafti S, Levdikov V, Antson AA, Bax B, Sanders CM (2019) Structural and functional analysis of the nucleotide
- 34 and DNA binding activities of the human PIF1 helicase. *Nucleic Acids Res* 47: 3208-3222
- 35 Ding Y, Fleming AM, Burrows CJ (2018) Case studies on potential G-quadruplex-forming sequences from the bacterial
- 36 orders Deinococcales and Thermales derived from a survey of published genomes. Sci Rep 8: 15679
- 37 Eddy J, Maizels N (2006) Gene function correlates with potential for G4 DNA formation in the human genome. *Nucleic*
- 38 Acids Res 34: 3887-3896
- 39 Eddy J, Maizels N (2008) Conserved elements with potential to form polymorphic G-quadruplex structures in the first
- 40 intron of human genes. *Nucleic Acids Res* 36: 1321-1333
- 41 Eddy S, Maddukuri L, Ketkar A, Zafar MK, Henninger EE, Pursell ZF, Eoff RL (2015) Evidence for the kinetic partitioning of
- 42 polymerase activity on G-quadruplex DNA. *Biochemistry* 54: 3218-3230

- 1 Edwards DN, Machwe A, Wang Z, Orren DK (2014) Intramolecular telomeric G-quadruplexes dramatically inhibit DNA
- 2 synthesis by replicative and translesion polymerases, revealing their potential to lead to genetic change. PLoS One 9:
- 3 e80664
- 4 Emsley P, Lohkamp B, Scott WG, Cowtan K (2010) Features and development of Coot. Acta crystallographica Section D,
- 5 *Biological crystallography* 66: 486-501
- 6 Fontana GA, Gahlon HL (2020) Mechanisms of replication and repair in mitochondrial DNA deletion formation. *Nucleic*
- 7 Acids Res 48: 11244-11258
- 8 Griffin BD, Bass HW (2018) Review: Plant G-quadruplex (G4) motifs in DNA and RNA; abundant, intriguing sequences of
- 9 unknown function. *Plant Sci* 269: 143-147
- 10 Heddi B, Cheong VV, Martadinata H, Phan AT (2015) Insights into G-quadruplex specific recognition by the DEAH-box
- 11 helicase RHAU: Solution structure of a peptide-quadruplex complex. Proceedings of the National Academy of Sciences of
- the United States of America 112: 9608-9613
- 13 Hossain KA, Jurkowski M, Czub J, Kogut M (2021) Mechanism of recognition of parallel G-quadruplexes by DEAH/RHAU
- helicase DHX36 explored by molecular dynamics simulations. Computational and structural biotechnology journal 19:
- 15 2526-2536
- 16 Hou XM, Wu WQ, Duan XL, Liu NN, Li HH, Fu J, Dou SX, Li M, Xi XG (2015) Molecular mechanism of G-quadruplex
- unwinding helicase: sequential and repetitive unfolding of G-quadruplex by Pif1 helicase. The Biochemical journal 466:
- 18 189-199
- Huppert JL, Balasubramanian S (2005) Prevalence of quadruplexes in the human genome. *Nucleic Acids Res* 33: 2908-
- 20 2916
- 21 Kabsch W (2010) XDS. Acta crystallographica Section D, Biological crystallography 66: 125-132
- Lee WTC, Yin Y, Morten MJ, Tonzi P, Gwo PP, Odermatt DC, Modesti M, Cantor SB, Gari K, Huang TT et al (2021) Single-
- 23 molecule imaging reveals replication fork coupled formation of G-quadruplex structures hinders local replication stress
- 24 signaling. *Nature communications* 12: 2525
- 25 Lemmens B, van Schendel R, Tijsterman M (2015) Mutagenic consequences of a single G-quadruplex demonstrate
- 26 mitotic inheritance of DNA replication fork barriers. *Nature communications* 6: 8909
- 27 Levitus M, Waisfisz Q, Godthelp BC, de Vries Y, Hussain S, Wiegant WW, Elghalbzouri-Maghrani E, Steltenpool J,
- 28 Rooimans MA, Pals G et al (2005) The DNA helicase BRIP1 is defective in Fanconi anemia complementation group J.
- 29 *Nature genetics* 37: 934-935
- 30 Li JH, Lin WX, Zhang B, Nong DG, Ju HP, Ma JB, Xu CH, Ye FF, Xi XG, Li M et al (2016) Pif1 is a force-regulated helicase.
- 31 Nucleic Acids Res 44: 4330-4339
- 32 Li SB, Wang HL, Jehi SA, Li J, Liu S, Wang Z, Truong L, Chiba T, Wang ZF, Wu XH (2021) PIF1 helicase promotes break-
- induced replication in mammalian cells. Embo J 40
- 34 Liu NN, Ji L, Guo Q, Dai YX, Wu WQ, Guo HL, Lu KY, Li XM, Xi XG (2020) Quantitative and real-time measurement of
- 35 helicase-mediated intra-stranded G4 unfolding in bulk fluorescence stopped-flow assays. Anal Bioanal Chem 412: 7395-
- 36 7404
- 37 Lovelace LL, Minor W, Lebioda L (2005) Structure of human thymidylate synthase under low-salt conditions. Acta
- 38 crystallographica Section D, Biological crystallography 61: 622-627
- 39 Lu KY, Chen WF, Rety S, Liu NN, Wu WQ, Dai YX, Li D, Ma HY, Dou SX, Xi XG (2018a) Insights into the structural and
- 40 mechanistic basis of multifunctional S-cerevisiae Pif1p helicase. *Nucleic Acids Res* 46: 1486-1500
- 41 Lu KY, Chen WF, Rety S, Liu NN, Wu WQ, Dai YX, Li D, Ma HY, Dou SX, Xi XG (2018b) Insights into the structural and
- 42 mechanistic basis of multifunctional S. cerevisiae Pif1p helicase. Nucleic Acids Res 46: 1486-1500
- 43 Lu KY, Xin BG, Zhang T, Liu NN, Li D, Rety S, Xi XG (2021) Structural study of the function of Candida Albicans Pif1.
- 44 Biochem Biophys Res Commun 567: 190-194
- 45 Maizels N, Gray LT (2013) The G4 genome. PLoS Genet 9: e1003468

- 1 McCoy AJ, Grosse-Kunstleve RW, Adams PD, Winn MD, Storoni LC, Read RJ (2007) Phaser crystallographic software. J
- 2 Appl Crystallogr 40: 658-674
- 3 Mendoza O, Bourdoncle A, Boulé J-B, Brosh RM, Jr, Mergny J-L (2016) G-quadruplexes and helicases. Nucleic Acids Res
- 4 44: 1989-2006
- 5 Paeschke K, Burkovics P (2021) Mgs1 function at G-quadruplex structures during DNA replication. Curr Genet 67: 225-
- 6 230
- Petoukhov MV, Franke D, Shkumatov AV, Tria G, Kikhney AG, Gajda M, Gorba C, Mertens HD, Konarev PV, Svergun DI
- 8 (2012) New developments in the ATSAS program package for small-angle scattering data analysis. J Appl Crystallogr 45:
- 9 342-350
- 10 Schierer T, Henderson E (1994) A protein from Tetrahymena thermophila that specifically binds parallel-stranded G4-
- 11 DNA. Biochemistry 33: 2240-2246
- 12 Schwindt E, Paeschke K (2018) Mms1 is an assistant for regulating G-quadruplex DNA structures. Curr Genet 64: 535-540
- 13 Singh DK, Ghosh AK, Croteau DL, Bohr VA (2012) RecQ helicases in DNA double strand break repair and telomere
- 14 maintenance. Mutation Research/Fundamental and Molecular Mechanisms of Mutagenesis 736: 15-24
- 15 Todd AK, Johnston M, Neidle S (2005) Highly prevalent putative quadruplex sequence motifs in human DNA. *Nucleic*
- 16 Acids Res 33: 2901-2907
- 17 Traczyk A, Liew CW, Gill DJ, Rhodes D (2020) Structural basis of G-quadruplex DNA recognition by the yeast telomeric
- protein Rap1. Nucleic Acids Res 48: 4562-4571
- 19 Varshney D, Spiegel J, Zyner K, Tannahill D, Balasubramanian S (2020) The regulation and functions of DNA and RNA G-
- 20 quadruplexes. Nature reviews Molecular cell biology 21: 459-474
- 21 Voter AF, Qiu Y, Tippana R, Myong S, Keck JL (2018) A guanine-flipping and sequestration mechanism for G-quadruplex
- 22 unwinding by RecQ helicases. *Nature communications* 9: 4201
- 23 Wang L, Wang QM, Wang YR, Xi XG, Hou XM (2018) DNA-unwinding activity of Saccharomyces cerevisiae Pif1 is
- 24 modulated by thermal stability, folding conformation, and loop lengths of G-quadruplex DNA. The Journal of biological
- 25 chemistry 293: 18504-18513
- 26 Wu CG, Spies M (2016) G-quadruplex recognition and remodeling by the FANCJ helicase. Nucleic Acids Res 44: 8742-
- 27 8753

- 28 Zhang W-Z, Tang J-C, Wang S-S, Wang Z-J, Qin W-M, He J-H (2019) The protein complex crystallography beamline
- 29 (BL19U1) at the Shanghai Synchrotron Radiation Facility. Nuclear Science and Techniques 30: 170
- 30 Zhou R, Zhang J, Bochman ML, Zakian VA, Ha T (2014) Periodic DNA patrolling underlies diverse functions of Pif1 on R-
- 31 loops and G-rich DNA. eLife 3: e02190
- 32 Zhou X, Ren W, Bharath SR, Tang X, He Y, Chen C, Liu Z, Li D, Song H (2016) Structural and Functional Insights into the
- Unwinding Mechanism of Bacteroides sp Pif1. *Cell reports* 14: 2030-2039
- 34 Zimmer K, Puccini A, Xiu J, Baca Y, Spizzo G, Lenz H-J, Battaglin F, Goldberg RM, Grothey A, Shields AF et al (2020) WRN-
- 35 Mutated Colorectal Cancer Is Characterized by a Distinct Genetic Phenotype. Cancers 12

#### 1 TABLES

# 2 Table 1. Binding and unwinding activities of *ToPif1* for different DNA substrates<sup>1</sup>.

Substrate		Binding <sup>2</sup>	Unwinding <sup>3</sup>		
	<del>-</del>	$K_{\rm d,app}$ (nM)	$A_{ m m}$	$k_{cat}$ (s <sup>-1</sup> )	4
	G4 <sup>CEB</sup>	23.27 ± 3.12	$\mathrm{ND}^4$	ND	5
D 11.1.CA	G4 <sup>P-214</sup>	ND	$0.55 \pm 0.02$	1.57 ± 0.07	6
Parallel G4	G4 <sup>P-241</sup>	ND	$0.35 \pm 0.02$	$1.23 \pm 0.05$	7
	G4 <sup>P-124</sup>	ND	$0.22 \pm 0.01$	1.17 ± 0.04	8
	G4 <sup>Tel</sup>	29.63 ± 2.64	ND	ND	<del>9</del> 10
Antiparallel G4	$G4^{AP-424}$	ND	$0.72 \pm 0.06$	$2.18 \pm 0.02$	11
_	4G4 <sup>AP-333</sup>	ND	$0.70 \pm 0.03$	$0.57 \pm 0.01$	12
ssDNA	$T_{12}$	29.12 ± 4.19	-	-	13
dsDNA	$S_{26}D_{17}$	ND	$0.59 \pm 0.02$	3.53 ± 0.02	14
Blunt-end DNA	$D_{24}$	250~280	-	-	15

<sup>&</sup>lt;sup>1</sup>Data were determined from 2-3 independent experiments under the experimental conditions as described in Materials

and Methods.

<sup>&</sup>lt;sup>2</sup>Data obtained from Fig 1A.

 $<sup>^3</sup>$ Parameters were fitted from Figs 1B and 6B. The original curve of ToPif1 unwinding substrate  $S_{26}D_{17}$  were not shown.

<sup>20 &</sup>lt;sup>4</sup>ND, not determined.

Table 2. Parameters of binding and unwinding activities of *ToPif1* and its variants<sup>1</sup>.

	G4 binding	G-quadru	plex unwinding		ssDNA binding	dsDNA un	winding	
	$(G4^{Tel})$	(AP-S	S <sub>16</sub> -TelG4)		$(T_{12})$	$(S_{26}D$	117)	
Variants	K <sub>d,app</sub> (nM)	$A_{\mathrm{m}}$	$k_{\rm cat}({\rm s}^{-1})$	$k_{\rm cat}/K_{ m d,app}^2$	K <sub>d,app</sub> (nM)	$A_{\mathrm{m}}$	$k_{\rm cat}({\rm s}^{\text{-}1})$	$k_{ m cat}/K_{ m d,app}^{3}$
ToPif1	29.63 ± 2.64	$0.53 \pm 0.01$	$0.48 \pm 0.01$	0.0162 ± 0.0012	30.20 ± 1.41	$0.59 \pm 0.02$	$3.53 \pm 0.02$	$0.1169 \pm 0.0031$
R392A	28.50 ± 2.20	$0.40 \pm 0.01$	$0.27 \pm 0.02$	$0.0095 \pm 0.0001$	28.30 ± 1.80	$0.32 \pm 0.01$	$3.50 \pm 0.02$	$0.1237 \pm 0.0067$
R355A	133.00 ± 18.04	$0.38 \pm 0.02$	$0.07 \pm 0.01$	$0.0005 \pm 0.0001$	38.10 ± 1.15	$0.34 \pm 0.01$	1.27 ± 0.01	$0.0333 \pm 0.0005$
R135A	119.00 ± 10.67	$0.34 \pm 0.02$	$0.05 \pm 0.01$	$0.0004 \pm 0.0001$	$30.90 \pm 0.47$	$0.47 \pm 0.01$	$1.42 \pm 0.02$	$0.0460 \pm 0.0010$
Q327A	$51.50 \pm 3.23$	$0.48 \pm 0.01$	$0.41 \pm 0.02$	$0.0080 \pm 0.0002$	63.40 ± 9.42	$0.43 \pm 0.03$	$6.14 \pm 0.03$	$0.0968 \pm 0.0121$
R419A	$38.50 \pm 2.25$	$0.24 \pm 0.02$	$0.21 \pm 0.01$	$0.0055 \pm 0.0001$	$38.20 \pm 5.47$	$0.32 \pm 0.02$	$2.46 \pm 0.01$	$0.0644 \pm 0.0016$
K329A	48.70 ± 2.65	$0.37 \pm 0.01$	$0.29 \pm 0.02$	$0.0060 \pm 0.0001$	$30.00 \pm 1.38$	$0.39 \pm 0.02$	$3.38 \pm 0.01$	$0.1127 \pm 0.0040$
R150A	152.00 ± 12.97	$0.28 \pm 0.01$	$0.06 \pm 0.01$	$0.0004 \pm 0.0001$	$31.30 \pm 1.76$	$0.43 \pm 0.03$	$2.50 \pm 0.01$	$0.0799 \pm 0.0039$
E397A	28.30 ± 2.21	$1.00 \pm 0.01$	1.19 ± 0.01	$0.0420 \pm 0.0027$	29.40 ± 1.36	$0.49 \pm 0.02$	$3.79 \pm 0.02$	$0.1289 \pm 0.0050$
E397L	$33.00 \pm 3.24$	$0.88 \pm 0.01$	1.18± 0.01	$0.0358 \pm 0.0020$	$36.00 \pm 2.84$	$0.48 \pm 0.01$	$2.36 \pm 0.02$	$0.0656 \pm 0.0043$
Е397Н	44.60 ± 1.68	$0.78 \pm 0.03$	1.32± 0.01	$0.0296 \pm 0.0009$	$50.90 \pm 3.45$	$0.31 \pm 0.02$	$2.64 \pm 0.02$	$0.0519 \pm 0.0030$
E397D	38.80 ± 8.07	0.45± 0.01	0.35± 0.02	$0.0090 \pm 0.0011$	$28.00 \pm 3.18$	$0.49 \pm 0.01$	$3.27 \pm 0.01$	0.1168 ± 0.0116

<sup>&</sup>lt;sup>1</sup>The reported data are the average values determined from 3-4 independent assays as performed under experimental conditions as described in 'Materials and Methods'.

<sup>&</sup>lt;sup>2</sup> The values are the equivalent ratios of  $k_{\text{cat}}$  (G-quadruplex unwinding) and  $K_{\text{d,app}}$  (G4 binding) comes from the data of Figs 1A, 5A and 6A.

<sup>&</sup>lt;sup>3</sup> The values are the equivalent ratios of  $k_{\rm cat}$  (dsDNA S<sub>26</sub>D<sub>17</sub> unwinding) and  $K_{\rm d,app}$  (ssDNA T<sub>12</sub> binding).

#### FIGURE LEGENDS

#### Figure 1. Binding and unwinding activities of ToPif1 for different configurations of antiparallel and parallel G4s.

- A Comparison of the binding activity of *ToP*if1 for different configurations of antiparallel (G4<sup>Tel</sup>, black points) and parallel (G4<sup>CEB</sup>, red points) G4s. (Insert: Comparison of the binding activity of *ToP*if1 to single-stranded DNA (T<sub>12</sub>, black points) with G4<sup>Tel</sup>, red points), the blue points represent of the double-strand DNA (D<sub>24</sub>)). The binding activity was measured using steady-state fluorescence anisotropy assays; 5 nM of fluorescein-labeled DNA substrate and 0.5 mM ADP·AlF<sub>4</sub> were titrated with increasing protein concentrations at 37 °C. The different binding curves represent an average of 3-4 independent experiments for each substrate with standard deviations. The solid line represents the fit of data according to Eq. (1).
- B Stopped-flow DNA unwinding kinetics of *ToP*if1 for different configurations of G4 DNA (G4<sup>AP-424</sup>, 4G4<sup>AP-333</sup>, G4<sup>P-214</sup>) under multiple turnover conditions. All curves represent the average of at least 10 individual traces and the plots are representative of three independent experiments. 4 nM G4 DNA and 100 nM *ToP*if1 were used under experimental conditions as described in 'Materials and Method'.
- C, D The typical smFRET trajectories of antiparallel (smG4<sup>AP-424</sup>, sm4G4<sup>AP-333</sup>) and parallel (smG4<sup>P-111</sup>) G4 unwinding catalyzed by 50 nM *To*Pif1 and 150 μM ATP. Black arrows in the solid style indicate the time of adding proteins. Dashed arrows in black represent the unwinding time of *To*Pif1 with different G4 DNA substrates.

#### Figure 2. Structure analysis of ToPif1 complexed with G-quadruplex (G4) DNA and ADP·AIF<sub>4</sub>.

- A Overall structure of *To*Pif1-G4<sup>T6/T8</sup>-ADP·AlF<sub>4</sub> ternary complex in cartoon mode with the conserved domains 1A (green), 1B (orange), 2A (pink), 2B (blue), and C-terminal (CTD, brown). G4 DNA (G4<sup>T6/T8</sup>) is colored in red and ADP·AlF<sub>4</sub> is shown as a black stick. *To*Pif1 molecules binding at the 5'- and 3'-ends of G4 DNA are labeled as molecule *a* and molecule *b*, respectively.
- B Surface view after cutting the crystal structure  $ToPif1-G4^{T6/T8}-ADP\cdot AIF_4$  ternary complex and the domains are colored as in (A).
- C Structural superposition for the structures of molecules *a* and *b* with the mass centers of domain 2B shown as a sphere (mass centers of molecules *a* colored in blue and that of molecules *b* colored in cyan).
- D Comparison of G4<sup>T6/T8</sup> (red) in the *To*Pif1 ternary complex, G4<sup>Myc</sup> (PDB: 5VHE (Chen *et al.*, 2018)) colored in cyan and G4 'T-loops' (PDB: 6LDM (Traczyk *et al*, 2020)) colored in yellow.
- Residues of the molecule a that interact with G4 layers in the  $ToPif1-G4^{T6/T8}-ADP\cdot AlF_4$  ternary complex; G4 DNA  $(G4^{T6/T8})$  is shown in red and the interacting residues are represented as sticks.

### Figure 3. Atomic interactions between the integral G-quadruplex (G4) DNA and ToPif1.

A Interactions of *ToPif1* and the G4 layer I.

- B The negative-negative repulsion interaction between E397 and the G7 of  $G4^{T6/T8}$  in the *ToPif1* ternary complex structure. The electrostatic potential at  $\pm$  5  $kTe^{-1}$  was colored in blue (basic/positive), white (neutral), and red (acidic/negative).
- C, D Interaction of ToPif1 and G4 layers II and III, respectively. Molecular electrostatic potential map calculated with G4 DNA omitted from the co-crystal structure (blue to red,  $\pm$  5  $kTe^{-1}$ ).

# Figure 4. Structural superposition of ToPif1 with the G4<sup>T6/T8</sup> and the GR<sub>17</sub>.

- A Interaction between *ToP*if1 and the T6 of G4<sup>T6/T8</sup> in the *ToP*if1-G4<sup>T6/T8</sup>-ADP·AlF<sub>4</sub> ternary complex.
- B Superposition on domain 1A of structures in *ToPif1-G4*<sup>T6/T8</sup> and *ToPif1-GR*<sub>17</sub>.
- C Interaction between *ToP*if1 and the G7 of GR<sub>17</sub> in the *ToP*if1-GR<sub>17</sub>-ADP·AlF<sub>4</sub> ternary complex.
- D Structural superposition of interacting residues for *ToP*if1 with the T6 of G4<sup>T6/T8</sup> and the G7 of GR<sub>17</sub>.

#### Figure 5. G-quadruplex (G4) unwinding activity of wild-type ToPif1 (ToPif1) and its mutants.

- A Stopped-flow kinetics of the G4 (AP-S<sub>16</sub>-TelG4) unwinding activity of *To*Pif1 and the various modified proteins. The different unwinding curves represent an average of 3-4 independent experiments for each substrate. The solid line represents the fit of data according to Eq. (2).
- B Bar plot of  $k_{\text{cat}}/K_{\text{d,app}}$  values in Table 2 (n=3 biological replicates). The  $k_{\text{cat}}/K_{\text{d,app}}$  values of G4 in descending numerical order (front panel), and these are determined with the dsDNA (S<sub>26</sub>D<sub>17</sub>, back panel). Data are presented as means  $\pm$  SD.
- C-F The typical smFRET trajectories of antiparallel G4 (smG4<sup>AP-424</sup>) unwinding catalyzed by different *To*Pif1 mutants based on single-molecular FRET assays. The dashed magenta, black, and red lines represent the states of G4: fully folded, incompletely folded, and fully unfolded, respectively. The concentrations of the R355A (C), R135A (D), R150A (E), and R419A (F) mutants were 50 nM with 150 µM ATP. The experimental conditions are described in Methods. Black arrows in the solid style indicate the time of adding proteins.

# Figure 6. Stimulating effect upon mutation of E397.

- A Stopped-flow kinetics of the antiparallel G4 (AP-S<sub>16</sub>-TelG4) unwinding activity of *To*Pif1 and its mutants. The different curves represent an average of 3-4 independent experiments for each substrate. The solid line represents the fit of data according to Eq. (2).
- B E397A mutant stimulating effect determined with parallel G4 DNA.
- C-E The typical FRET trajectories of antiparallel G4 (smG4<sup>AP-424</sup>) unwinding catalyzed by a different point mutations on E397 using single-molecular FRET assays. The dashed magenta and red lines represent the fully folded and unfolded states of G4, respectively. The different unwinding curves represent an average of 3-4 independent experiments for each substrate. Black arrows in the solid style indicate the time of adding proteins.

Error bar plot of unwinding time of E397A, E397L, and E397H determined from unfolding curves of (C), (D), and (E), respectively (n=3 biological replicates). The experimental conditions are described in Materials and Methods and data are presented as means ± SD.

#### **Expanded View FIGURE LEGENDS**

#### Figure EV1. To Pif1 recognition for G4 and ssDNA.

- A CD experiments of G4 DNA.
- B Left panel: DNA binding of ToPif1 to G4<sup>CEB</sup> with 1 μM T<sub>12</sub> (black line) or 1μM G4<sup>CEB</sup> (blue line) or none of them (red line). The binding of Fitting of the data to the Eq.1 yields a  $K_{d,app}$  value for ToPif1-G4<sup>CEB</sup> of 30.30 ± 1.17 nM, a  $K_{d,app}$  value for ToPif1-G4<sup>CEB</sup> (added with 1 μM T<sub>12</sub>) of 30.91 ± 2.32 nM. Right panel: DNA binding of ToPif1 to T<sub>12</sub> with 1 μM G4<sup>CEB</sup> (red line) or 1 μM T<sub>12</sub> (blue line) or none of them (black line). Fitting of the data to the Eq.1 yields a  $K_{d,app}$  value for ToPif1-T<sub>12</sub> of 29.10 ± 0.53 nM, a  $K_{d,app}$  value for ToPif1-T<sub>12</sub> (added with 1 μM G4<sup>CEB</sup>) of 26.50 ± 0.71 nM. DNA binding assays were carried out in buffer A (25 mM Tris-HCl (pH 7.5), 50 mM NaCl, 2 mM MgCl<sub>2</sub> and 2 mM DTT) with 0.5 mM ADP·AlF<sub>4</sub>.
- C Stopped-flow unwinding kinetic curves of *ToPif1* unwinding G4 DNA (G4<sup>AP-424</sup>, G4<sup>P-214</sup>, 4G4<sup>AP-333</sup>) in buffer A with 1 mM ADP·AlF<sub>4</sub>.
- D CD analysis of G4<sup>AP-424</sup> and G4<sup>P-214</sup>.
- E Normalized melting curves from CD melting assays for G4<sup>AP-424</sup> and G4<sup>P-214</sup> at different temperatures (20-75°C).
- F Cartoon representation of ToPifl (molecule a) with  $G4^{T6/T8}$  in the presence of  $ADP \cdot AlF_4$  shown as a black stick and loop3 highlighted in magenta.
- G Cartoon representation of *ToPif1-dT*<sub>15</sub>-ADP·AlF<sub>4</sub> (PDB: 6S3M (Dai *et al.*, 2021)) with ADP·AlF<sub>4</sub> shown as a black stick and loop3 highlighted in magenta.
- H Cartoon representation of *Ba*Pif1-dT<sub>10</sub>- ADP·AlF<sub>4</sub> (PDB: 5FHE (Zhou *et al.*, 2016)) with ADP·AlF<sub>4</sub> shown as a black stick and loop3 highlighted in magenta.
- I Cartoon representation of *Sc*Piflp-poly (G3T5)-ADP·AlF<sub>4</sub> (PDB: 5O6B (Lu *et al*, 2018b)) with ADP·AlF<sub>4</sub> shown as a black stick and loop3 highlighted in magenta.

# Figure EV2. Comparison of domain 2B of the molecule *a* of the *To*Pif1-G4<sup>T6/T8</sup>-ADP·AIF<sub>4</sub> ternary complex and the previously determined *To*Pif1-ss/dsDNA structure (PDB: 6S3H (Dai *et al.*, 2021)).

A Cartoon representation of molecule a in the  $ToPif1-G4^{T6/T8}-ADP\cdot AIF_4$  structure with domain 2B and the center mass (sphere) of domain 2B is highlighted in blue. G-quadruplex (G4) DNA is shown in red.

- B Cartoon representation of the *ToP*if1-S<sub>7</sub>D<sub>11</sub>-ADP·AlF<sub>4</sub> structure (PDB: 6S3H (Dai *et al.*, 2021)) with domain 2B shown in magenta. The center mass of domain 2B is shown as a red sphere.
- C Superposition on domain 1A of the structures in (A) and (B).
- D Domain 2B and G4 DNA of molecule *a* in the *To*Pif1-G4<sup>T6/T8</sup>-ADP·AlF<sub>4</sub> structure with the close-up view of interactions between *To*Pif1 and the G4 tetrad I.
- E Domain 2B and modeled duplex DNA in the ToPif1-S<sub>7</sub>D<sub>11</sub>-ADP·AIF<sub>4</sub> structure (PDB: 6S3H (Dai et al., 2021)).
- F Superposition on domain 1A of the structure in (C) with only domain 2B and G4 DNA being shown.

# Figure EV3. SAXS results of ToPif1-G4<sup>T6/T8</sup>-ADP·AlF<sub>4</sub>.

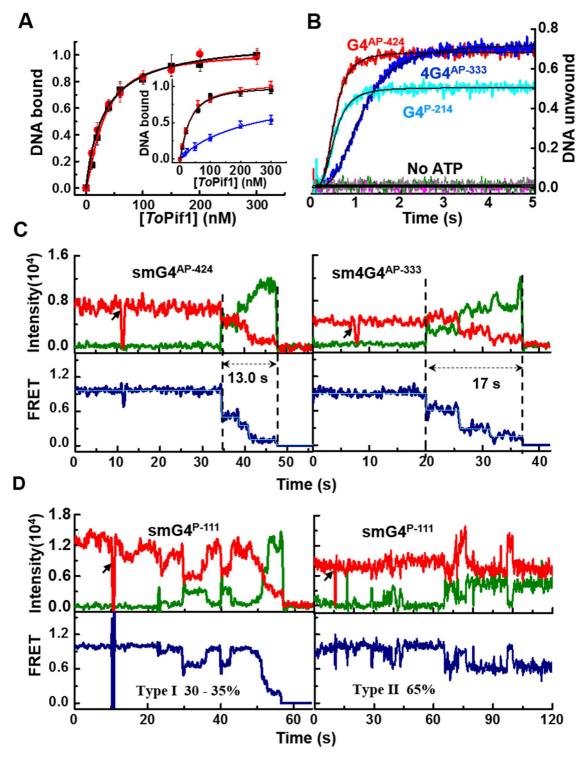
- A Fit curve of the SAXS data of ToPif1- G4<sup>T6/T8</sup>-ADP·AlF<sub>4</sub> with two modeled ToPif1 molecules bound to the substrate G4<sup>T6/T8</sup> calculated with Crysol.
- B The model of *ToP*if1- G4<sup>T6/T8</sup>-ADP·AlF<sub>4</sub> superimposed on the *ab initio* envelope calculated with DAMMIF.
- C The SAXS Model of *To*Pif1-G4<sup>T6/T8</sup> -ADP·AlF<sub>4</sub>.
- D Crystal structure of *ToPif1-G4*<sup>T6/T8</sup> -ADP·AlF<sub>4</sub>.
- E Superposition for SAXS model and crystal structure of *To*Pif1-G4<sup>T6/T8</sup> -ADP·AlF<sub>4</sub>.

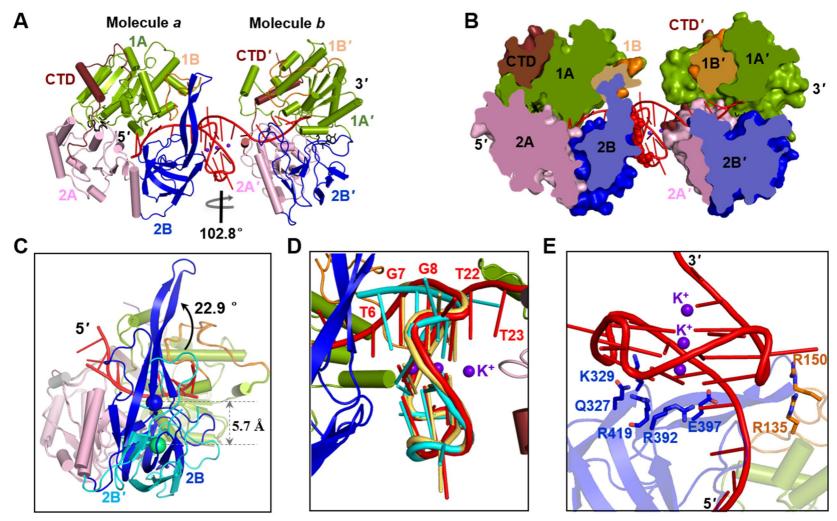
# Figure EV4. Functional validation of *ToPif1* mutants and ligand interaction diagram of T6/G7 in the *ToPif1* complex compared with the guanine-specific pocket (GSP) in the *CsRecQ* structure.

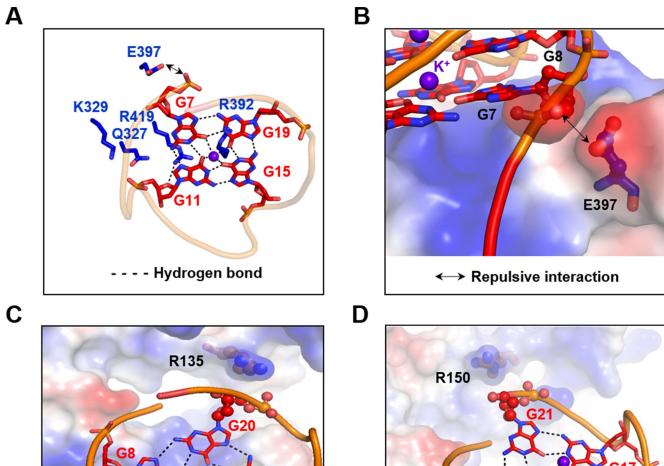
- A CD results of ToPif1 and its mutants.
- B ATP hydrolysis of ToPif1 and its mutants with or without DNA effector ( $S_{18}H_{11}$ ).
- C Ligand interaction between T6 and *To*Pif1 in the *To*Pif1-G4<sup>T6/T8</sup>- ADP·AlF<sub>4</sub> structure.
- D Ligand interaction between G7 and ToPif1 in the ToPif1-GR<sub>17</sub>- ADP·AlF<sub>4</sub> structure (PDB: 7BIL (Dai et al., 2021)).
- E Ligand interaction between G21 and CsRecQ in CsRecQ-ssDNA structure (PDB: 6CRM (Voter et al., 2018)).

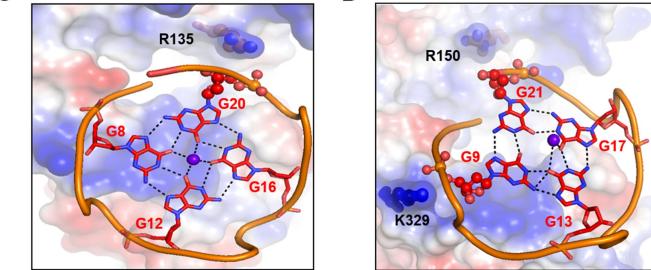
#### Figure EV5. Sequence alignment of Pif1 helicase from bacteria, humans, and yeast.

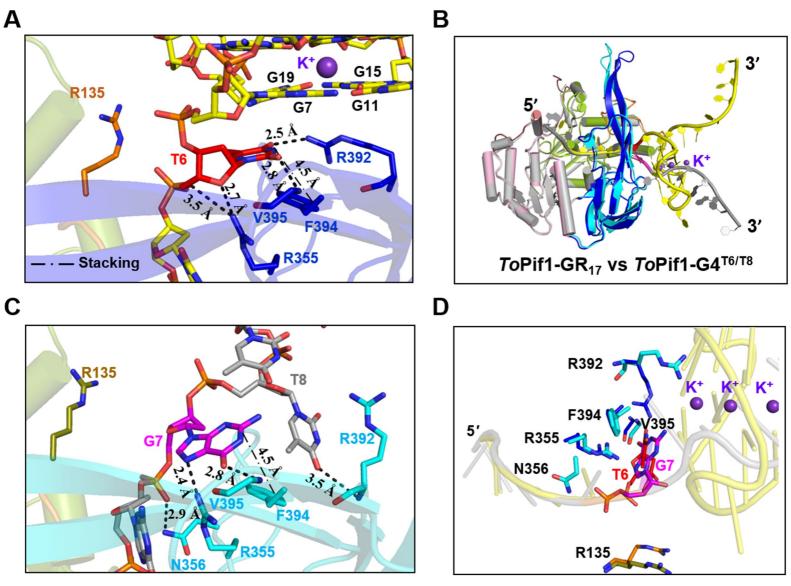
Thermus bacteria Pifl (1-8) are from *Thermus oshimai* (*To*Pifl), *Thermodesulfovibrio yellowstonii* (*Ty*Pifl), *Sulfurihydrogenibium sp* (*Su*Pifl), *Anaerobaculum hydrogeniformans* (*Ah*Pifl), *Thermodesulfobacterium commune* (*Tc*Pifl), *Deferribacter desulfuricans* (*De*Pifl), *Mycolicibacterium thermoresistibile* (*Mt*Pifl), *Synergistales bacterium* (*Sb*Pifl). Bacteria at room temperature are from *Bacteroides sp* (*Bs*Pifl). Homo sapiens and *Saccharomyces cerevisiae* are labeled as *Hs*Pifl and *Sc*Pifl. Residues involved in G4-Recognizing Surface (GRS) are shown with green stars.

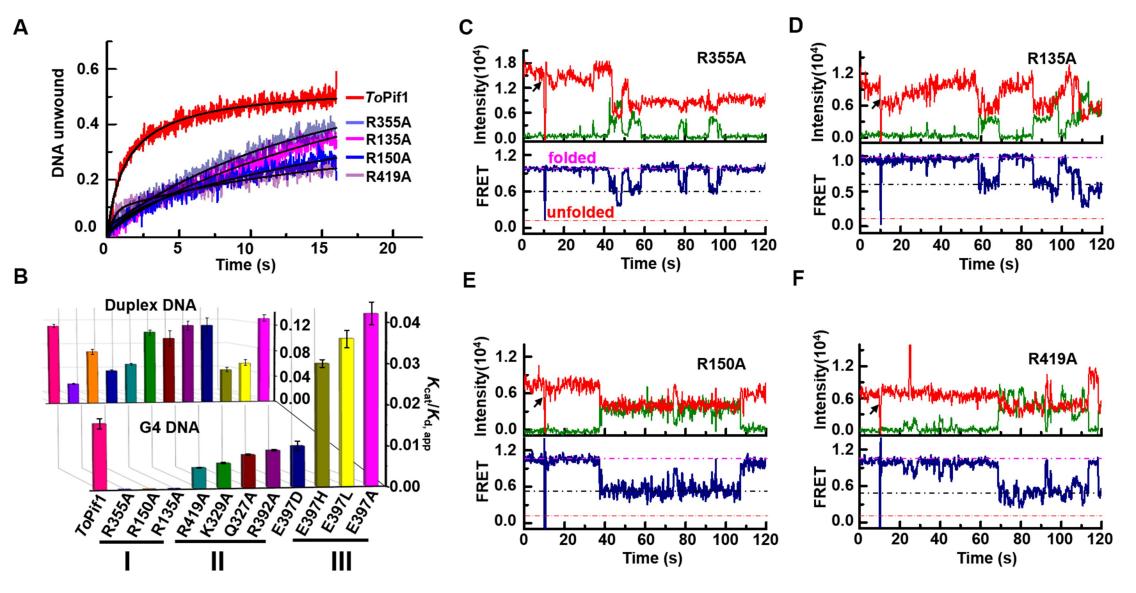


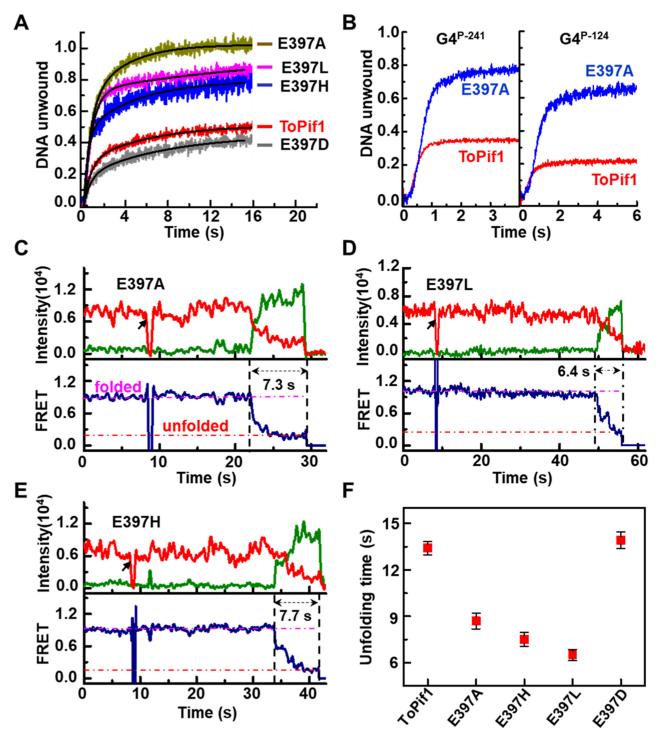


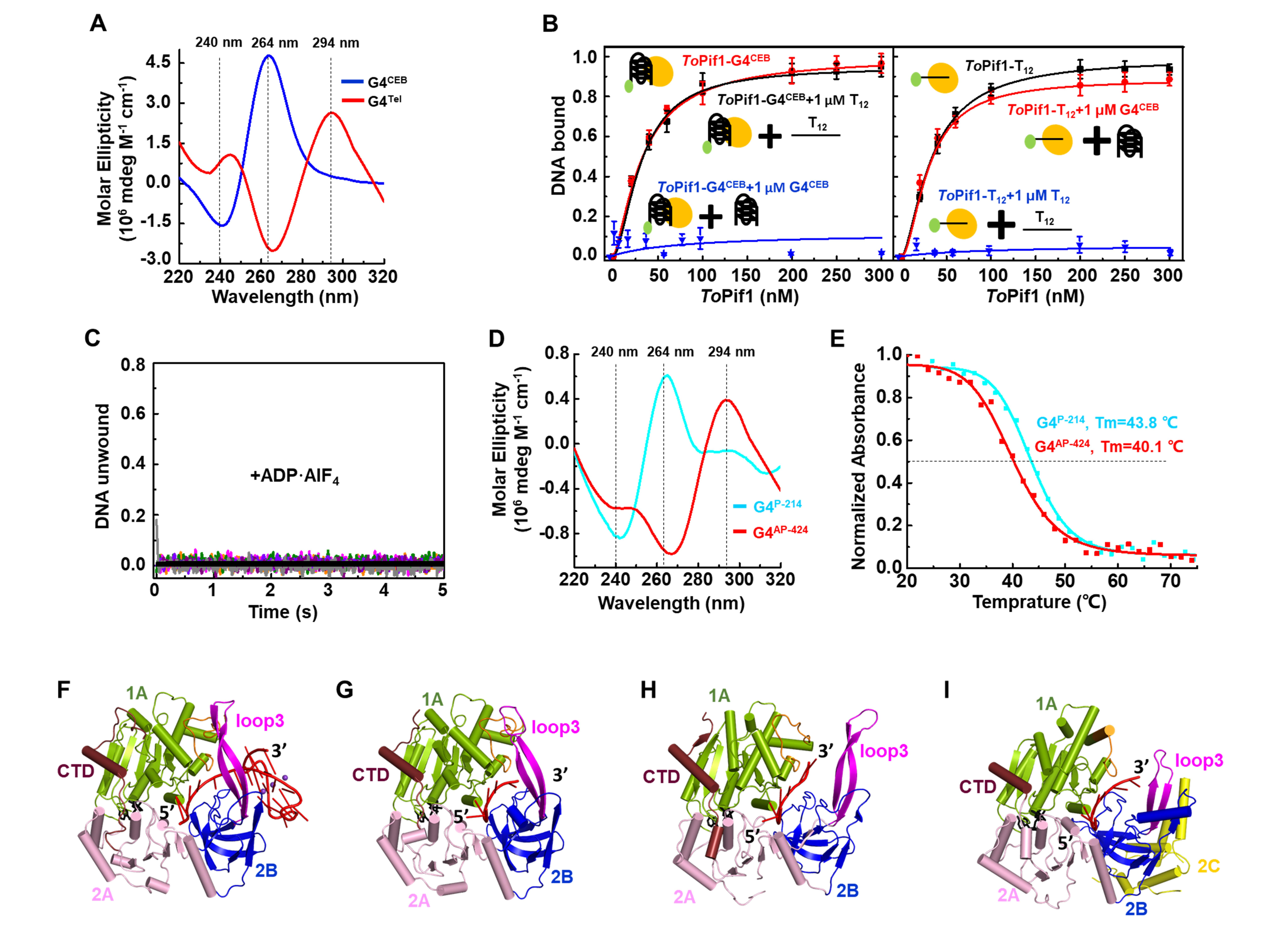


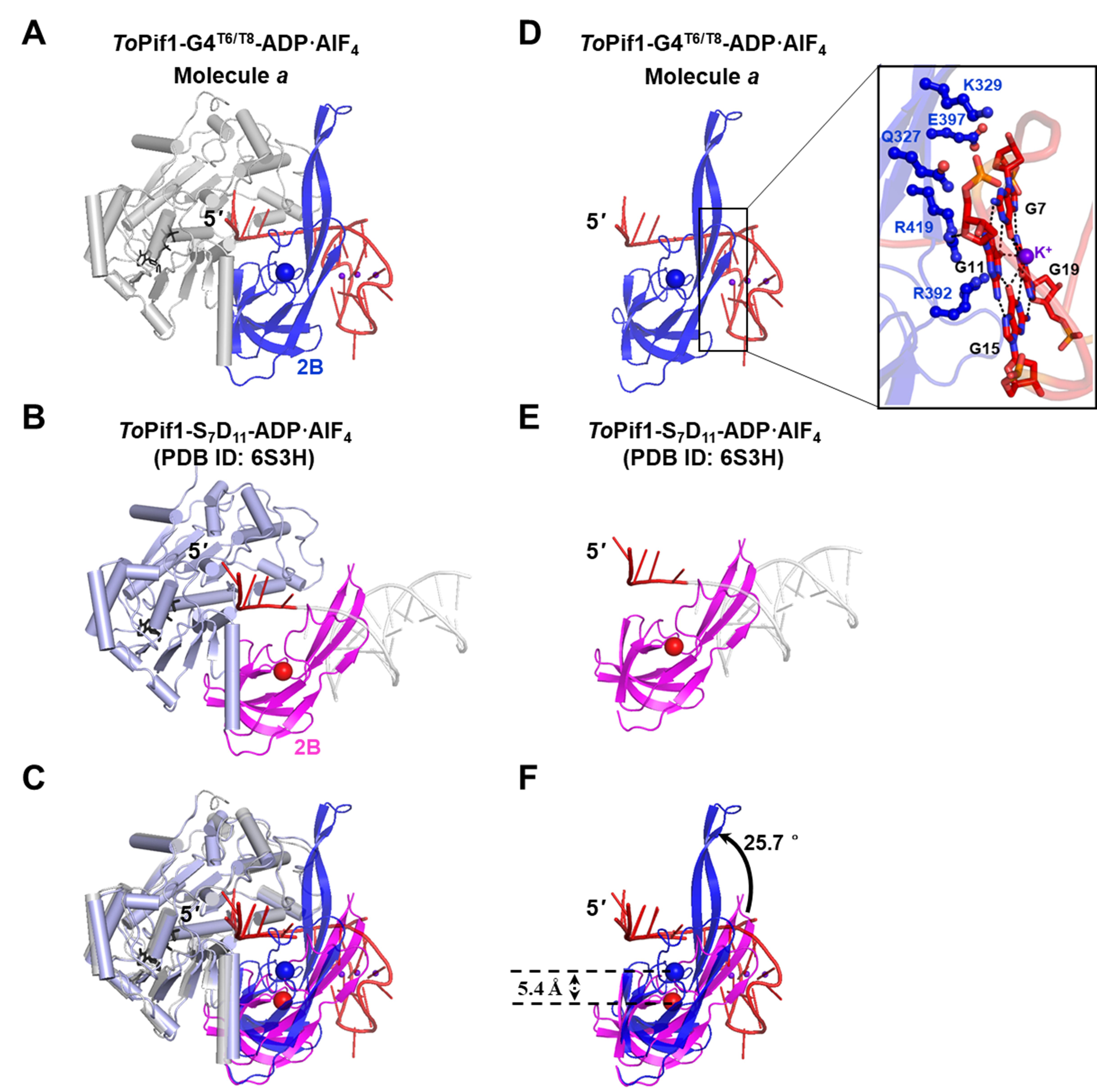


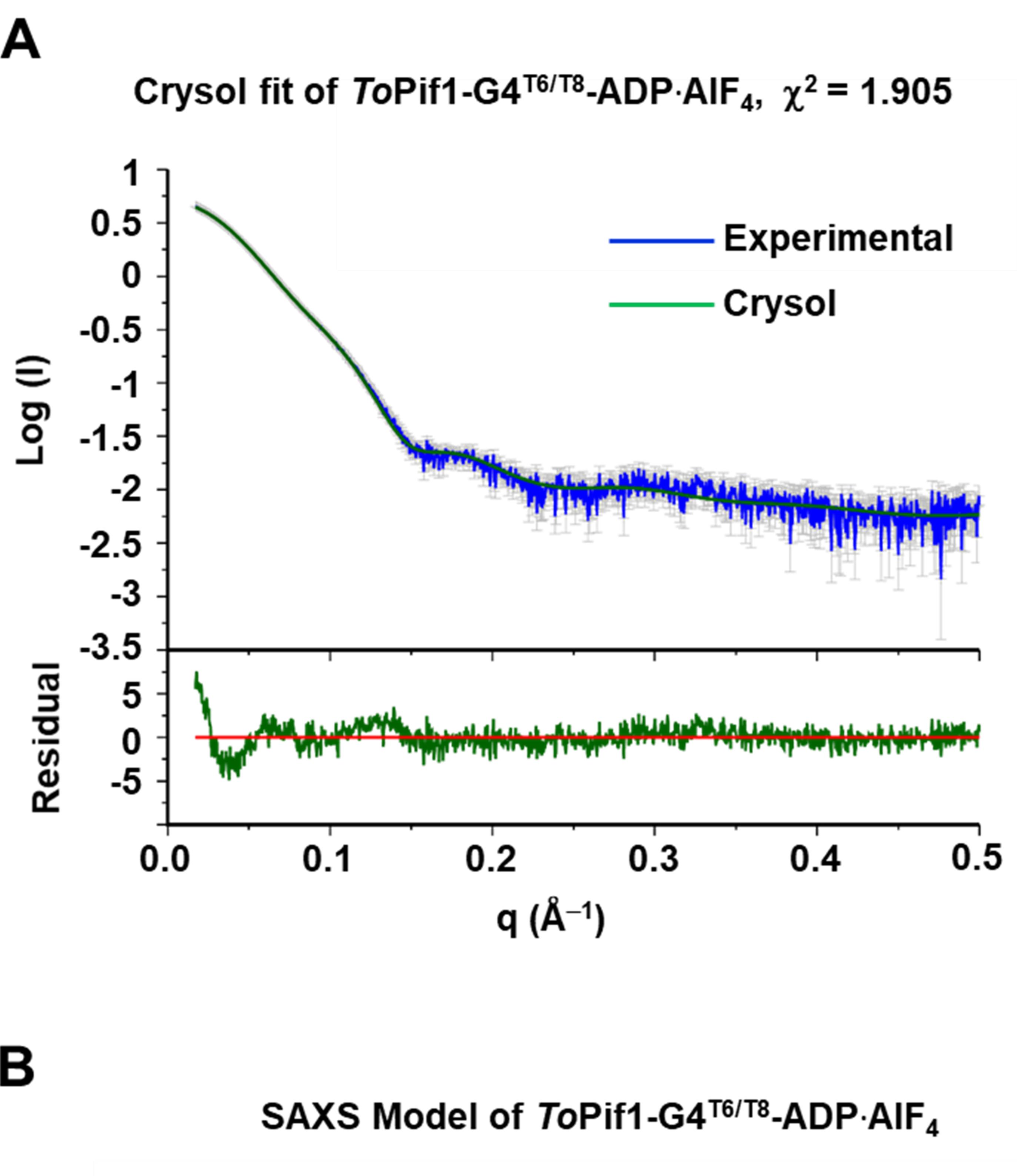












SAXS Model of ToPif1-G4T6/T8-ADP·AIF<sub>4</sub>

